Spin Torque Gate Magnetic Field Sensor

Hang Xie,[1] Xin Chen,[1] Ziyan Luo,[1,2] and Yihong Wu[1,*]

[1] *Department of Electrical and Computer Engineering, National University of Singapore, Singapore 117583, Singapore*

[2] *School of Physics and Electronics, Central South University, Changsha 410083, China*

(Received 7 November 2020; revised 12 January 2021; accepted 29 January 2021; published 17 February 2021)

Spin-orbit torque provides an efficient pathway to manipulate the magnetic state and magnetization dynamics of magnetic materials, which is crucial for energy-efficient operation of a variety of spintronic devices, such as magnetic memory, logic, oscillator, and neuromorphic computing. Here, we describe and experimentally demonstrate a strategy for the realization of a spin torque gate magnetic sensor with an extremely simple structure by exploiting the longitudinal field dependence of the spin torque driven magnetization switching. Unlike most magnetoresistance sensors, which require a delicate magnetic bias to achieve a linear response to the external field, the spin torque gate sensor can achieve the same without any magnetic bias, which greatly simplifies the sensor structure. Furthermore, by driving the sensor using an ac current, the dc offset is automatically suppressed, which eliminates the need for a bridge or compensation circuit. We verify the concept using the $WTe_2/Ti/(Co, Fe)B$ trilayer and demonstrate that the sensor can work linearly in the range of ±3–10 Oe with negligible dc offset.

DOI: 10.1103/PhysRevApplied.15.024041

I. INTRODUCTION

When a charge current passes through a ferromagnet (FM)-heavy metal (HM) bilayer, spin-orbit torque (SOT) is induced, which is exerted on the magnetization of the FM layer [1–5]. In general, there are two main mechanisms that contribute to the generation of SOT in FM/HM bilayers: one is the interfacial Rashba-Edelstein effect [1,6,7] and the other is the bulk spin Hall effect [2,8–12]. The relative contribution of the two mechanisms in generating the SOT depends on both the constituent materials and nature of the interface. Irrespective of the mechanisms, it is now commonly accepted that there are two types of SOTs, one is fieldlike (FL) and the other is dampinglike (DL), which may be expressed as $\vec{T}_{\rm FL} = \tau_{\rm FL}\vec{m} \times (\vec{j} \times \vec{z})$ and $\vec{T}_{\rm DL} = \tau_{\rm DL}\vec{m} \times [\vec{m} \times (\vec{j} \times \vec{z})]$, respectively, where $\vec{m}$ is the magnetization direction; $\vec{j}$ is the in-plane current density; $\vec{z}$ is the interface normal; and $\tau_{\rm FL}$ and $\tau_{\rm DL}$ are the magnitude of the FL and DL torques, respectively [5,13–15]. The DL torque provides an efficient mechanism for switching the magnetization of the FM with perpendicular magnetic anisotropy (PMA), as already demonstrated in numerous works [5]. In general, an assistive field parallel to the current direction is required to achieve deterministic switching (hereafter, we assume that the current is in the x direction, and thus, the required field component is H_x) [16]. As this requirement is undesirable for memory and logic applications, several approaches for achieving field-free switching have been reported [3,17–21]. Here, we demonstrate that this undesirable feature of SOT-based magnetization switching can be effectively exploited for magnetic field sensor applications.

The proposed sensor, which we term a spin torque gate (STG) or a stochastic magnetic field sensor, can be implemented in a simple Hall bar or Hall cross structure made of a FM/HM bilayer with PMA. When the bilayer is driven by an ac current, the strength and polarity of H_x will determine the duration within which magnetization will stay in the up and down states, respectively, in each half-cycle of the ac current. The average anomalous Hall effect (AHE) voltage gives an output signal that is proportional to H_x in the low-field range with zero offset. Since the output signal can be obtained from the average Hall voltage over many cycles, it statistically reduces the low-frequency noise. The STG sensor does not require any magnetic bias, which is the main cause of high costs associated with all types of magnetoresistance sensors, including anisotropic magnetoresistance, giant magnetoresistance, and tunnel magnetoresistance sensors [22–29]. To experimentally demonstrate the sensor, we develop a $WTe_2/Ti/(Co, Fe)B$ trilayer structure, the effective PMA of which can be tuned over a wide range by varying the temperature. This allows us to demonstrate the proof-of-concept operation of the STG sensor in both the deterministic switching and stochastic switching regimes. Despite the extremely simple structure, the sensor exhibits a good linearity in the field range of

[*] elewuyh@nus.edu.sg

$\pm$3–10 Oe, which is almost 10 times larger than the spin Hall magnetoresistance (SMR) sensor demonstrated by us previously that uses the FL effective field as the built-in linearization mechanism [30–34].

II. OPERATION PRINCIPLE AND EXPERIMENTAL DETAILS

A. Operation principle of the spin-torque gate and stochastic magnetic field sensor

The proposed sensor exploits the longitudinal field dependence of the magnetization reversal process of a FM/HM bilayer with PMA. Since the switching mechanism depends strongly on the size and effective PMA ($K_{\perp}^{\text{eff}}$) of the device, we consider the following three cases separately: (1) a single domain device with a sizable $K_{\perp}^{\text{eff}}$, (2) a large device that allows domain-wall (DW) nucleation and propagation, and (3) a device with a superparamagnetic FM layer.

The SOT-induced magnetization switching in case 1 may be described by a macrospin model [16], which predicts a critical current density of [35]

$$J_c = \frac{\sqrt{2}e}{\hbar}\frac{M_s t_{\text{FM}}}{\theta_{\text{SH}}}\left(\frac{H_k^{\text{eff}}}{\sqrt{2}} - |H_x|\right). \tag{1}$$

Here, M_s (t_{FM}) is the saturation magnetization (thickness) of the FM layer, H_k^{eff} is the effective anisotropy field, θ_{SH} is the effective spin Hall angle, H_x is the longitudinal field applied in the current direction, e is the electron charge, and $\hbar$ is the reduced Planck constant. We now consider an ac current $I(t)$ with the commonly used sine, sawtooth, and triangle waveforms, passing through the FM/HM bilayer [Fig. 1(a)]. The amplitude and period of the current are I_0 and T, respectively. The critical current I_c, which is the product of J_c and the cross-section area of the device (S), is shown in Fig. 1(a) as dashed lines. The corresponding AHE waveform $R_H(t)$ is shown in Fig. 1(b), which includes possible offset R_0 due to misalignment of the Hall voltage electrodes. When sketching the AHE waveform, we assume that it is positive when $I \geq I_c$ and $H_x > 0$ and negative when $I \leq -I_c$ and $H_x > 0$ (note: $I_c > 0$). The polarity will be reversed when H_x changes sign. It is interesting to note that the duty ratio of R_H for sine and triangular waves is always 50%, while for the sawtooth wave the duty ratio is dependent on I_c. Figure 1(c) shows the Hall voltage $V_H(t) = I(t)R_H(t)$ for different ac waveforms. It is clear that $V_H(t)$ is a periodic signal with the same period T of the ac current. When $H_x \ll H_k^{\text{eff}}$, the time average of the Hall voltage, $V_{\text{out}} = \frac{1}{T}\int_0^T V_H(t)dt$, is given by

$$V_{\text{out}} = \begin{cases} \dfrac{\sqrt{2}R_{\text{AHE}}S}{\pi}\dfrac{2e}{\hbar}\dfrac{M_s t_{\text{FM}}}{\theta_{\text{SH}}}\text{sgn}(H_x)\sqrt{\sqrt{2}H_k^{\text{eff}}|H_x|}, & \text{sine wave} \\ \dfrac{R_{\text{AHE}}S}{\sqrt{2}}\dfrac{2e}{\hbar}\dfrac{M_s t_{\text{FM}}}{\theta_{\text{SH}}}H_x, & \text{sawtooth wave} \\ \dfrac{R_{\text{AHE}}S}{\sqrt{2}}\dfrac{2e}{\hbar}\dfrac{M_s t_{\text{FM}}}{\theta_{\text{SH}}}H_x, & \text{triangular wave} \end{cases} \tag{2}$$

where R_{AHE} is the amplitude of $R_H(t)$. In all three cases, we set $I_0 = (e/\hbar)(M_s t_{\text{FM}}\text{SH}_k^{\text{eff}}/\theta_{\text{SH}})$ to remove the zero-field offset. The detailed derivation of Eq. (2) can be found in Appendix A. The average output signal as a function of H_x is shown in Fig. 1(d), which is nonlinear for a sine wave, but linear for the sawtooth and triangle waves. Equation (2) is the central result of this work; it demonstrates that it is possible to realize a linear magnetic field sensor without any magnetic bias, when the sensor is driven by either a sawtooth or triangle ac current. In addition, it is also not necessary to use a bridge to remove the zero-field offset. When the current amplitude is large enough, a very small change in H_x will lead to an increased or decreased probability of the magnetization being switched to one of the two directions, depending on the polarity of the field. Therefore, in principle, the sensor can be used for sensing a small field. As the way the signal is derived resembles the fluxgate sensor, we term it a STG magnetic field sensor. We also examine the case of the square wave, but, as explained in Appendix A, the square wave would lead to a constant amplitude of V_{out} independent of H_x (Fig. 12).

The macrospin model is valid for single-domain devices. For devices with lateral dimensions larger than the DW width (case 2), magnetization switching occurs primarily through domain-wall nucleation followed by propagation, which results in a much smaller critical current density [5,16,36–46]. The DW nucleation may occur either inside the film due to defects or at the edge of the sample due to the combined effect of the Dzyaloshinskii-Moriya interaction (DMI), the applied field and current, the demagnetizing field and thermal effect, etc. [5]. The latest studies suggest that DW nucleation at the edges plays

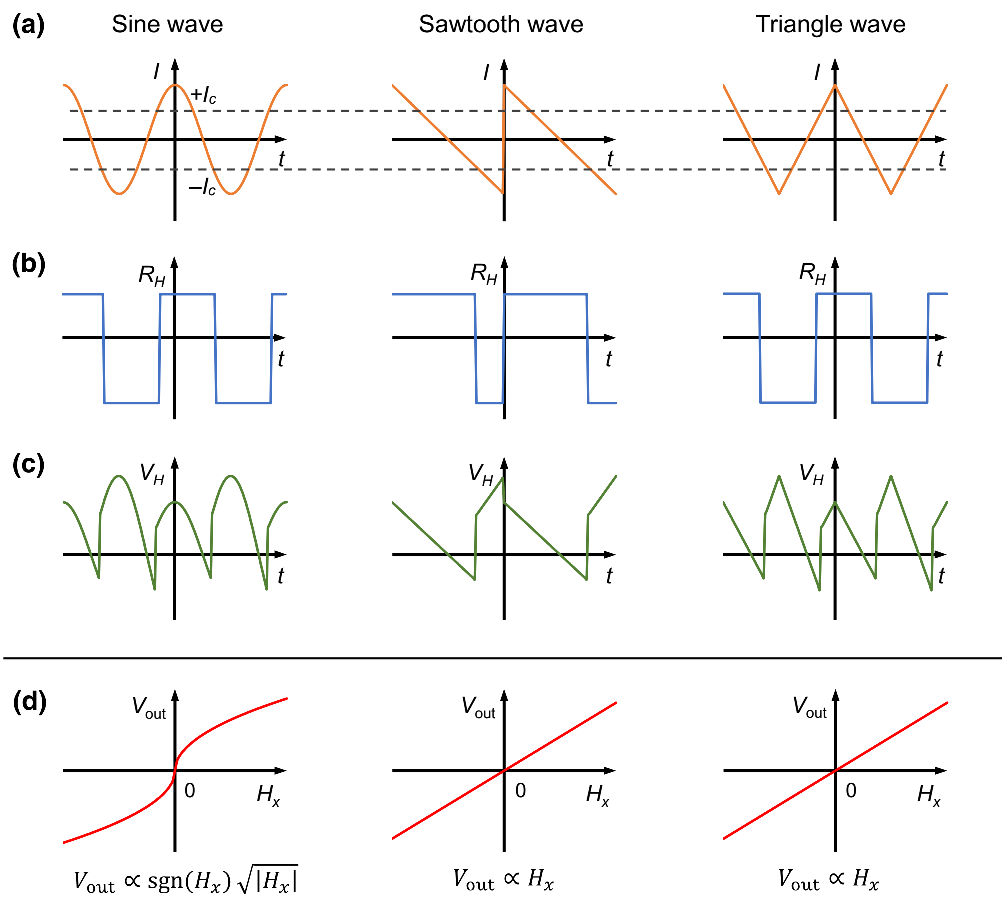

FIG. 1. (a)–(c) Current I, Hall resistance R_H, and Hall voltage V_H as a function of time for sine, sawtooth, and triangle waves. (d) Output voltage V_{out} as a function of in-plane field H_x for different ac currents.

a dominant role in reproducible and deterministic switching of magnetization. According to Pizzini *et al.* [43], the nucleation field at the edge may be written as

$$H_{n,\,\text{edge}} = \frac{\pi(\sigma_0 \mp 2\Delta\mu_0 M_s H_x)^2 t_{\text{FM}}}{4\mu_0 M_s p k_B T}.$$

Here, $\sigma_0 = 4\sqrt{AK_0} - D\pi$ is the domain-wall energy density in the presence of the DMI, D is the DMI constant, K_0 is the effective anisotropy constant, A is the exchange constant, $\Delta = \sqrt{A/K_0}$, μ_0 is the vacuum susceptibility, k_B is the Boltzmann constant, T is the temperature, and $p = \ln(\tau/\tau_0)$ with τ being waiting time and τ_0 the attempt time. When $H_x \ll (\sigma_0/2\Delta\mu_0 M_s) \approx (2K_0/\mu_0 M_s)$ (when D is small), one has

$$H_{n,\,\text{edge}} \approx \frac{4\pi A t_{\text{FM}}}{p k_B T}\left(\frac{H_k^{\text{eff}}}{2} \mp |H_x|\right). \tag{3}$$

Here, the $\mp$ sign indicates the nucleation site at opposite edges. In the actual case, only the minus sign is relevant, as DW propagation immediately follows nucleation. Since $p k_B T$ can be made much larger than $4\pi A t_{\text{FM}}$, this explains why the switching current density in DW-driven switching is much smaller than the value predicted by the macrospin model. When the nucleation field originates from the DL effective field, the corresponding critical current density may be written as

$$J_{c,\,\text{DW}} = \frac{4\pi e}{\hbar}\frac{M_s A t_{\text{FM}}^2}{p\theta_{\text{SH}} k_B T}\left(\frac{H_k^{\text{eff}}}{2} - |H_x|\right). \tag{4}$$

Equation (4) is essentially the same as that of Eq. (1), except for the prefactor. The prefactor can be further modified by taking the domain-wall pinning effect into consideration. Therefore, Eq. (2) is still applicable in the incoherent switching case.

Next, we look at case 3, i.e., when the effective anisotropy becomes very small. In this case, for a single-domain element, magnetization fluctuates between $+M_z$ and $-M_z$ due to weak PMA and small thermal stability. When it is used as the free layer of the magnetic tunnel junction, it results in a superparamagnetic or stochastic tunnel junction, which is an important building block for stochastic and neuromorphic computing [47–51]. Here, we explore its applications in sensors. Similar to the case of a spin with two directions pointing either parallel or antiparallel to the external field, when a magnetic field is applied along the easy axis of a superparamagnetic element with weak PMA, the average magnetization in the field direction may be written as $M_z = M_s \tanh(M_s H_z V/k_B T)$, and the Hall resistance is thus given by $R_H = R_0 + R_{\mathrm{AHE}} \tanh(M_s H_z V/k_B T)$. Here, H_z is the applied field along the easy axis, and V is the magnetic volume. When H_z is derived from the DL SOT effective field, we have $H_z^{\mathrm{DL}} = H^{\mathrm{DL}} m_x$ (H^{DL} is the magnitude of the DL effective field at $m_x = 1$). When H_x is small, we may write $H_z^{\mathrm{DL}} = (H^{\mathrm{DL}}/H_k^{\mathrm{eff}})H_x$, with $H^{\mathrm{DL}} = (\hbar/2e)(\theta_{\mathrm{SH}}/M_s t_{\mathrm{FM}} S)I$. From the above relationships, we can obtain the Hall voltage at small H_x as

$$V_H(t) = IR_0 + I^2 R_{\mathrm{AHE}} \frac{\hbar\theta_{\mathrm{SH}}}{2ek_B T}\frac{H_x}{H_k^{\mathrm{eff}}}. \tag{5}$$

When the sensor is driven by a sine wave $I = I_0 \cos\omega t$, the time average of $V_H(t)$ is given by

$$V_{\mathrm{out}} = I_0^2 R_{\mathrm{AHE}} \frac{\hbar\theta_{\mathrm{SH}}}{4ek_B T}\frac{H_x}{H_k^{\mathrm{eff}}}, \tag{6}$$

which presents a linear relationship with H_x with zero offset. In addition, a linear response can also be obtained when it is driven by other ac waveforms, namely, square, sawtooth, and triangle waves (see Appendix B). It is important to note that, in this case, the sensor is a spin torque gated stochastic magnetic field sensor. The gating operation is important because it eliminates the dc offset and, at the same time, also suppresses magnetic noise. Although the stochastic magnetic field sensor has been reported before, it is implemented using a stochastic flip-flop, which requires complex circuitry to ensure linearity and accuracy [52]. In contrast, the sensor presented here is extremely simple and comprises of only a single Hall device made of a FM/HM bilayer.

B. Sample preparation and experimental methods

All materials, except for Ti, are deposited on SiO_2 (300 nm)/Si substrates using magnetron sputtering with a base and working pressure of $<1 \times 10^{-8}$ and 1.5–3×10^{-3} Torr, respectively. The Ti layer is deposited by *e*-beam evaporation in the same vacuum system with the sputter without breaking the vacuum. Standard photolithography and liftoff techniques are used to fabricate the Hall bars. The Microtech laser writer system, with a 405 nm laser, is used to directly expose the photoresist (Microposit S1805), after which it is developed in MF319 to form the Hall bar pattern. After film deposition, the photoresist is removed by a mixture of Remover PG and acetone to complete Hall bar fabrication.

The surface roughness and sputtering rate of thin films are characterized using a Veeco Dimension 3100 AFM system. The magnetic properties are characterized using the Quantum Design MPMS3 system, with a resolution of $<1 \times 10^{-8}$ emu. The electrical measurements are performed in the Quantum Design VersaLab PPMS with a sample rotator. The ac or dc current is applied by the Keithley 6221 current source. The longitudinal or Hall voltage is measured by the Keithley 2182 nanovoltmeter (for dc voltage), the 500 kHz MFLI lock-in amplifier from Zurich Instruments (for harmonic voltage), or the National Instruments Data Acquisition (DAQ) device (for acquiring the voltage with a large sampling rate of 1 MHz).

III. RESULTS AND DISCUSSION

A. Current-induced switching of WTe_2/Ti/(Co, Fe)B at different temperatures

The STG sensor can be realized experimentally using any types of FM/HM bilayers, or even a single-layer FM, as long as it has a well-defined PMA, sizable dampinglike SOT, and the requirement of a longitudinal field for deterministic switching. We choose to use WTe_2(5)/Ti(2)/(Co, Fe)B(1.5)/MgO(2)/Ta(1.5) (the numbers in parentheses indicate the layer thicknesses in nm) for experimental implementation of the STG sensor because WTe_2 is reported to have a large charge-spin conversion efficiency [53–59]. Moreover, recently two groups have observed evident SOT in WTe_2 thin films prepared by sputtering [58,59], which is of more practical relevance when it comes to device applications. The (Co, Fe)B layer exhibits well-defined PMA in the multilayer structure, which arises mainly from the interface anisotropy of (Co, Fe)B/MgO [60], and the 2 nm Ti insertion layer functions, as a seed layer to promote the PMA [61,62]. The other consideration for using this structure is that its coercivity varies strongly with temperature, which, in addition to the STG sensor, also allows a spin torque gated stochastic magnetic sensor to be realized when the coercivity becomes very weak.

Smooth WTe_2 thin films with a root-mean-square (rms) roughness of about 0.2 nm are obtained by process optimization. The resistivity of the WTe_2 thin film at room temperature is around 8.7×10^3 $\mu\Omega$ cm, which is two orders of magnitude larger than the resistivity of normal metals. The increase in resistivity upon decreasing the temperature indicates the nonmetallic behavior of sputtered WTe_2. The highly resistive WTe_2 thin film is advantageous for sensor applications, since a larger anomalous Hall resistance will be obtained due to lower current shunting in WTe_2, if the overall power consumption will not increase due to the large charge-spin conversion efficiency in WTe_2. We further characterize the SOT in WTe_2-based ferromagnetic heterostructures by using the harmonic Hall measurements. The WTe_2-thickness-dependence study of SOT in WTe_2 ($t_{\mathrm{WTe_2}}$)/(Co, Fe)B (hereafter MgO(2)/Ta(1.5) is omitted for simplicity) is conducted, from which the DL SOT efficiency is found to have a negative sign and peak at around $t_{\mathrm{WTe_2}} = 5$ nm with a value of 0.67×10^5 Ω^{-1} m^{-1}. Only a slight decrease of the SOT is observed after a thin Ti layer is inserted between WTe_2 and (Co, Fe)B layers, which suggests the high spin transparency of Ti [61–63]. With the current distribution in each layer taken into account, the DL SOT field for the $WTe_2(5)/Ti(2)/(Co, Fe)B(1.5)$ stack is estimated to be 26.3 Oe per 10^7 A/cm^2, which is comparable to the value reported previously in a sputtered $WTe_2/Mo/(Co, Fe)B$ structure [59].

Figure 2(a) shows the schematic of a Hall bar device used for both electrical characterization and sensor demonstration. The Hall bar length, width, spacing between voltage electrodes, and width of voltage electrode are 120, 15, 30, and 5 μm, respectively. To estimate the effective anisotropy, we measure the $M-H$ curve of the $WTe_2(5)/Ti(2)/(Co, Fe)B(1.5)$ film by sweeping the field in the x direction [Fig. 2(b)] in a superconducting quantum interference device, from which the saturation magnetization and effective anisotropy field are obtained as 550 emu/cm^3 and $H_k^{\text{eff}} = 500$ Oe at room temperature, and 650 emu/cm^3 and $H_k^{\text{eff}} = 1000$ Oe at 200 K. This gives an effective anisotropy energy of 0.28×10^6 and 0.65×10^6 erg/cm^3 at room temperature and 200 K, respectively, corresponding to thermal stability factors of around 6 and 22, respectively (assuming the domain size is 40 nm). This allows us to demonstrate a proof-of-concept STG sensor in both the DW-driven (low-temperature) and stochastic (high-temperature) regions using the same device. Figure 2(c) shows the AHE curves at different temperatures, ranging from 160 to 300 K. As can be seen, the device exhibits well-defined PMA at low temperature and superparamagnetic behavior near room temperature with the coercivity ranging from 0 to 25 Oe and R_{AHE} in the range of 6.8–11.7 Ω. Furthermore, Fig. 2(d) shows the current-induced switching loops of the same sample at different temperatures with an assistive field, H_x, of ±30 Oe. As can be seen, the switching loops corroborate well the DL SOT-induced switching mechanism, with the switching polarity determined by both the current and H_x directions. Additionally, the opposite switching polarity in $WTe_2/Ti/(Co, Fe)B$, compared with Pt/Co [16,40,64], indicates a negative sign of the spin Hall angle in WTe_2, which is consistent with the results of SOT measurements. The switching current, I_{sw}, of $WTe_2(5)/Ti(2)/(Co, Fe)B(1.5)$ at $H_x = \pm 30$ Oe, defined as the current that switches 95% of the magnetization, is around 8 mA (3 mA) at 160 K (300 K), corresponding

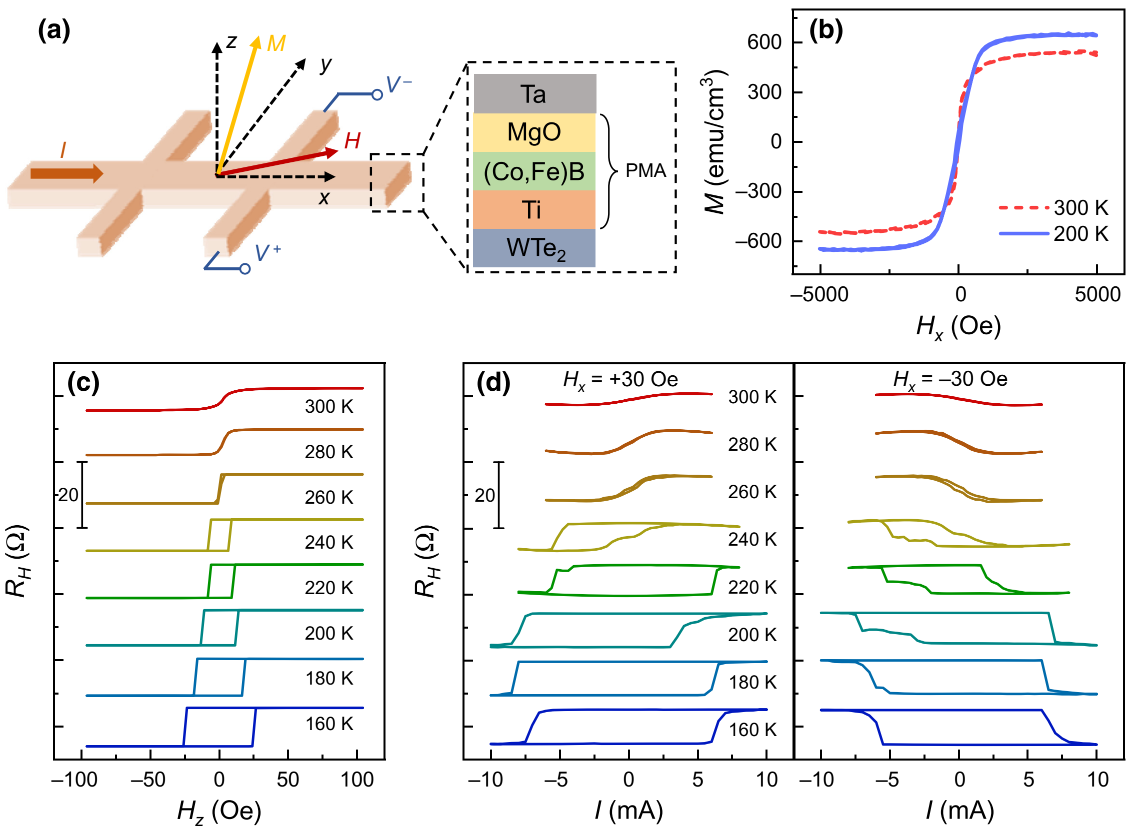

FIG. 2. (a) Schematic of the Hall bar device and electrical measurement configuration. (b) $M-H$ loops of $WTe_2(5)/Ti(2)/(Co, Fe)B(1.5)$ film at 200 and 300 K, respectively, with the field swept in the x direction. (c) AHE curves of $WTe_2(5)/Ti(2)/(Co, Fe)B(1.5)$ measured with a perpendicular field, H_z, and a small dc current of 200 μA at different temperatures from 160 to 300 K. (d) Current-induced switching loops of $WTe_2(5)/Ti(2)/(Co, Fe)B(1.5)$ at different temperatures with an in-plane assistive field, H_x, of $+30$ and -30 Oe. Pulse width of the pulse current is fixed at 2 ms.

to a current density of 1.33×10^7 A/cm^2 (5×10^6 A/cm^2). At low temperature, the switching is quite abrupt in the initial phase, but it becomes gradual in the final phase, indicating that switching is dominated by DW nucleation and propagation or expansion from the nucleation sites. The DW-dominated switching mechanism becomes more apparent at intermediate temperature, as manifested in multiple-step switching. The irregular hysteresis loop suggests that switching evolves from DW-driven to stochastic mode at around 240 K. This unique characteristic of $WTe_2(5)/Ti(2)/(Co, Fe)B(1.5)$ facilitates the demonstration of a STG sensor at low temperature and a spin torque gated stochastic sensor at room temperature.

B. Experimental demonstration of the STG magnetic field sensor

To demonstrate the proof-of-concept operation of the STG sensor, we apply an ac current with triangle or sawtooth waveforms with a frequency of 115 Hz to the device at 160 K and measure the time-averaged Hall voltage as a function of H_x. The Hall voltage is measured using a DAQ device. Figures 3(a) and 3(b) show the Hall voltage, V_H, of the sensor as a function of time captured by the DAQ device driven by the triangle and sawtooth waveforms, respectively, with a current amplitude of 8 mA and H_x of 100 Oe. As can be seen, Figs. 3(a) and 3(b) resemble the simulated $V_H - t$ curves displayed in Fig. 1(c). To achieve good sensor performance, we set the amplitude of the applied ac current as 11.5 mA. The output voltage V_{out} at each field is averaged over 1×10^6 sampling points for a duration of 1 s (corresponding to 115 cycles of ac current wave). Figure 3(c) shows the time-averaged V_{out} of the sensor in response to H_x swept forth and back between -3 and 3 Oe driven by a triangle wave. A linear response with <2.5% linearity error (as shown in the lower-right inset), a sensitivity of 167.7 mΩ/Oe, nearly zero dc offset, and negligible hysteresis is obtained. The upper-left inset in Fig. 3(c) shows the $V_{\mathrm{out}} - H_x$ dependence over a larger range from -10 to 10 Oe. It is worth pointing out that data shown in Fig. 3(c) are raw data without any dc offset compensation. Both the zero-dc offset and small hysteresis are unique features of the STG sensor, despite the fact that the sensor element has a finite coercivity, and there is always a dc offset in the AHE signal due to misalignment of the

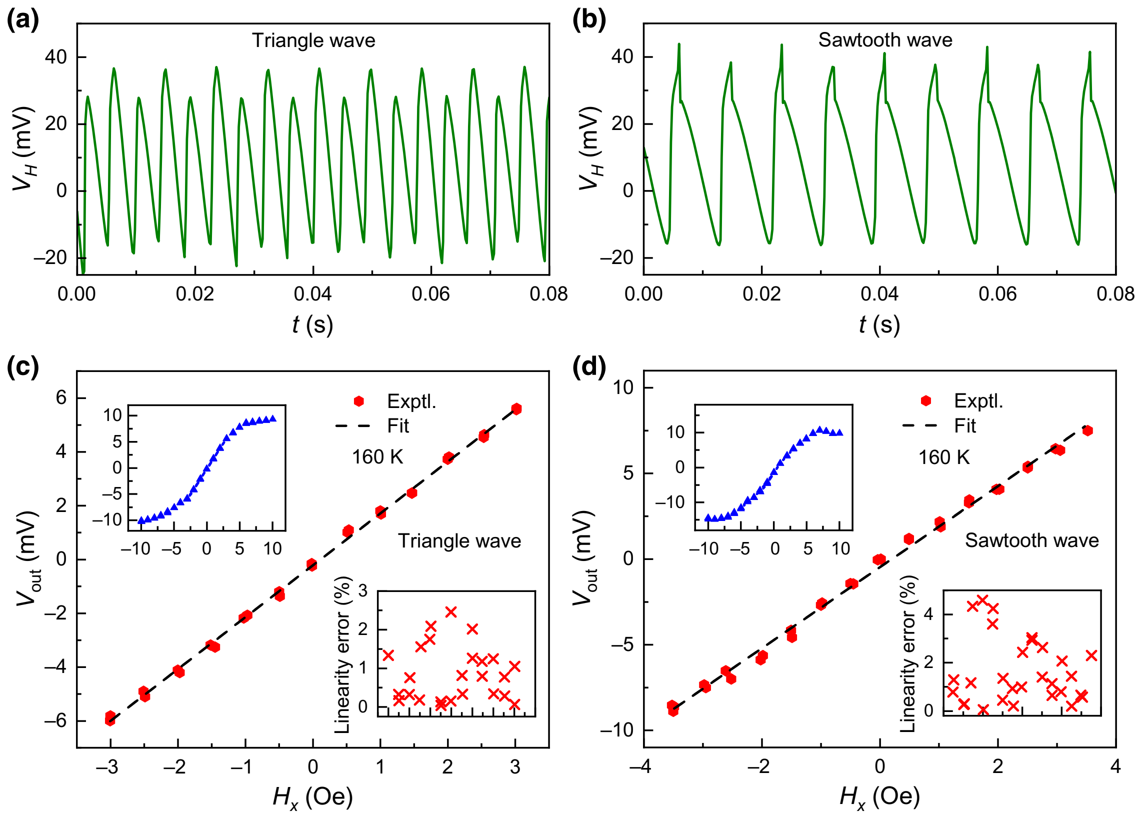

FIG. 3. (a),(b) Hall voltage V_H of the sensor as a function of time captured by the DAQ device driven by the sawtooth wave and triangle wave, respectively. (c) Output voltage V_{out} of the sensor in response to an external field H_x swept forth and back between -3 and 3 Oe driven by a triangle wave at 160 K. (d) V_{out} of the sensor in response to H_x swept forth and back between -3.5 and 3.5 Oe driven by a sawtooth wave at 160 K. Dashed line is a guide for the eye. Upper-left insets in (c),(d), output response curve over a larger sweeping range. Lower-right insets in (c),(d), linearity error within the sweeping field range.

Hall voltage probes. Similar results are also obtained using the sawtooth wave as the driving current. As shown in Fig. 3(d), the linear range and sensitivity are ±3.5 Oe and 205.5 mΩ/Oe, respectively, both of which are at similar levels to those of the triangle-wave case.

Next, we turn to the performance of the sensor at room temperature. As shown in Fig. 2(c), the hysteresis of this sample almost disappears when $T > 260$ K, although the sample still shows PMA. Since the lateral size of the active element of the sensor is 15×5 μm^2 (width of the Hall bar × width of the voltage electrode), we may reasonably postulate that there are a finite number of superparamagnetic elements inside the region that contribute to the AHE signal. If the dispersion of effective anisotropy is not that large, the overall M_z dependence on temperature should still follow the $M_z = M_s \tanh(M_s H_z V/k_B T)$ relation. The $R_H - I$ curves at 300 K can be well fitted using the hyperbolic tangent function $R_H = R_{\mathrm{AHE}} \tanh(I/I_c)$, where I_c is the critical current after which R_H starts to saturate. Therefore, we should be able to verify the proposed spin torque gated stochastic sensor using the same $\mathrm{WTe_2}$(5)/Ti(2)/(Co, Fe)B(1.5) device at room temperature.

Based on the aforementioned discussion, in this case, the amplitude of the ac current is not required to be larger than the critical current due to the absence of hysteresis. Figure 4 shows V_{out} of the sensor in response to H_x swept forth and back between −10 and 10 Oe driven by a square wave with an amplitude of 2 mA and frequency of 115 Hz. The upper-left inset displays the output response curve over a larger sweeping range (−30 to 30 Oe), which shows the saturation of the output signal in the high-field range. The linearity error within the field range of ±10 Oe is less than 2%, as shown in the lower-right inset, indicating a good linearity of the sensor. The sensitivity of this device at room temperature is 102 mΩ/Oe. Based on a linearity error of less than 5%, the minimum detectable field for this sensor is 0.1 Oe at 160 K and 0.02 Oe at 300 K (see Appendix C), which can be improved by optimizing the materials, layer structure, and dimensions of the sensor. The other possible approach is to replace the AHE-based signal read-out by a magnetic tunnel junction. In this case, the signal amplitude can be increased by at least 1–2 orders, and therefore, we can anticipate a significant improvement of the field detectivity. Although the stray field from the fixed layer in the out-of-plane direction may slightly reduce the sensor's sensitivity, as discussed in Sec. III D, it can be mitigated by suppressing the stray field via structure optimization.

C. Frequency dependence of the STG sensor performance

Since the sensor is driven by an ac current, it is instructive to estimate its frequency dependence. First, there should be an optimum frequency range for the driving

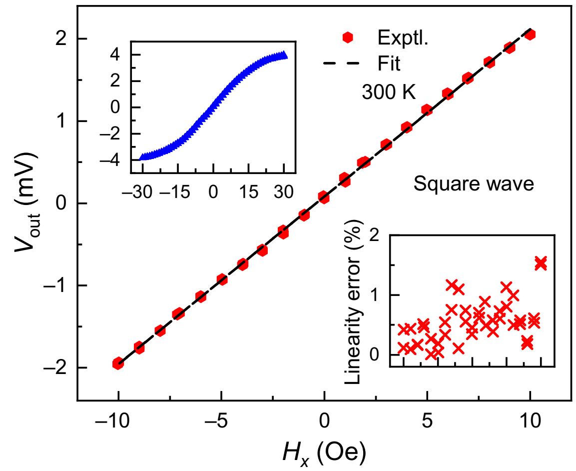

FIG. 4. V_{out} in response to H_x swept forth and back between −10 and 10 Oe at 300 K (dashed line is a guide for the eye). Upper-left inset, output response curve over a larger sweeping range. Lower-right inset, linearity error within the sweeping field range.

current. This is because, on the one hand, the increased frequency will result in an increased switching current due to the reduced duration at each current cycle, a well-established fact for SOT-based magnetization switching, and, on the other hand, we need a minimum number of cycles to reduce the noise of the output signal, which sets the lower limit for the driving current frequency. As pertaining to the present experiment, the minimum frequency is limited by the sampling duration of the DAQ device, i.e., the frequency which allows the DAQ device to average at least 10 current cycles, meaning that, if the sampling duration is 1 s, the lowest frequency will be 10 Hz. We first measured the sensor response in the current frequency range from 15 to 10 015 Hz at 160 K (case 2). The minimum frequency of 15 Hz is selected to guarantee a reasonable number of cycles for averaging within the sampling duration. Figures 5(a)–5(c) show the sensor output response with a fixed current amplitude of 11.5 mA and different current frequencies of 15, 515, and 2015 Hz, respectively. As can be seen, the linearity degrades as the frequency increases. In addition, there is a large hysteresis at 2015 Hz. Therefore, the current frequency has an evident effect on the sensor performance. Degradation of the linearity at higher frequency can be explained by incomplete switching due to the decreased duration at each current cycle, which is similar to the pulse-width effect on current-induced switching, i.e., a smaller pulse width will lead to a larger switching current. Therefore, for practical applications, one may have to optimize the current amplitude and frequency concurrently.

For case 3, since the amplitude of the ac current is not required to be larger than the critical current due to the

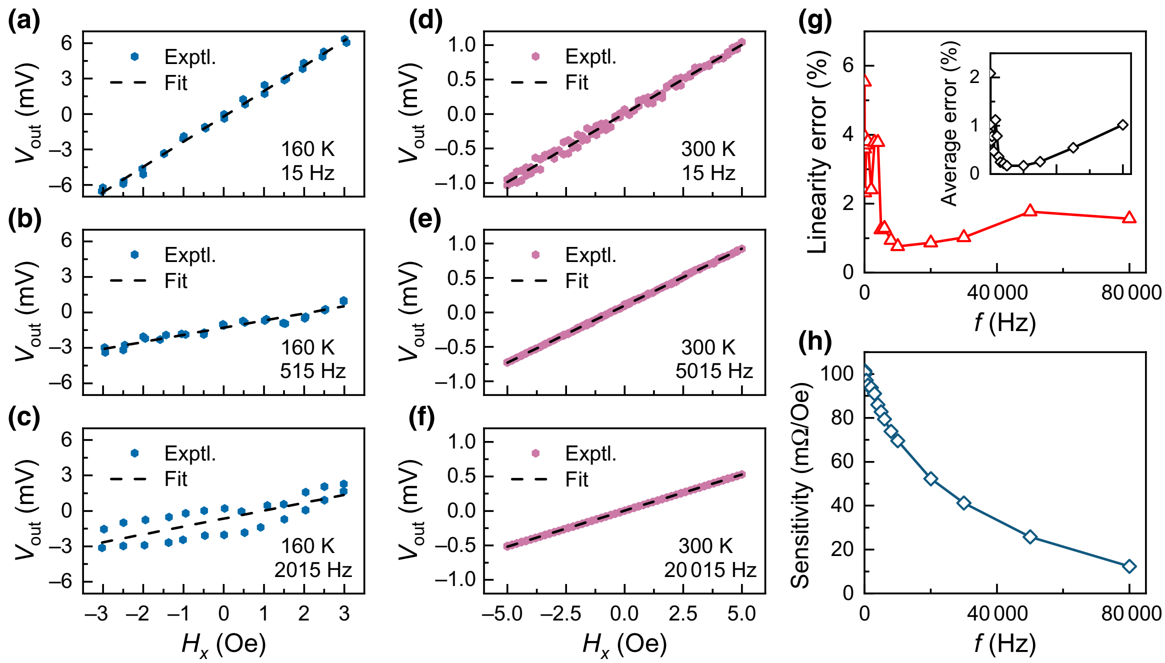

FIG. 5. (a)–(c) V_{out} in response to H_x swept forth and back between −3 and 3 Oe at 160 K with current frequencies of 15, 515, and 2015 Hz, respectively. (d)–(f) V_{out} in response to H_x swept forth and back between −5 and 5 Oe at 300 K with current frequencies of 15, 5015, and 20 015 Hz, respectively. Dashed line is a guide for the eye. (g) Maximum and average (inset) linearity error. (h) Sensitivity within the field range as a function of current frequency from 15 to 80 015 Hz at 300 K.

absence of hysteresis, the sensor performance may not be degraded as much as in the previous case at high frequency. To confirm this, we perform the measurements at 300 K with different current frequencies from 15 to 80 015 Hz (the highest current frequency of the Keithley 6221 system is 100 kHz) in a Helmholtz coil, with a field range of −5 Oe–5 Oe and a field step of 0.2 Oe. Figures 5(d)–5(f) show the output voltage in response to H_x at a fixed current amplitude of 2 mA and current frequency of 15, 5015, and 20 015 Hz, respectively. As can be seen, different from case 2, the sensor response shows a good linearity at all three frequencies. In addition, it can be observed that both the linearity error and sensitivity decrease as the frequency increases. By further plotting the linearity error (maximum value), average error, and sensitivity of the sensor versus the current frequency from 15 to 80 015 Hz, as shown in Figs. 5(g) and 5(h), we find that the linearity error and average error overall decrease from 15 to 10 015 Hz, reaching a very low level at 10 015 Hz, after which both experience a slight increase. On the other hand, the sensitivity keeps decreasing as the frequency increases; this is due to the increase in switching current, as discussed above. The decreased linearity error at high frequency is because more cycles are averaged within the sampling duration. The slight increase of linearity error after10 015 Hz might be due to the constant decrease of output amplitude. Therefore, for case 3, the sensor can be operated over a wide frequency range.

Next, we turn to the frequency limitation of the detection field. In principle, it is limited by both the sensor driving frequency and the DAQ sampling duration. A detailed analysis of the relationship between them is ongoing, but in what follows we provide a few sets of measurement results to illustrate the frequency effect. We test the sensor response to an ac field supplied by the Helmholtz coil at 300 K. The field amplitude is fixed at 0.5 Oe, and the field frequency, f_H, is varied from 0.1 to 1 Hz. The current amplitude and frequency of the sensor's driving current are 2 mA and 20 015 Hz, respectively. The DAQ sampling duration is set as 0.1 s. Figures 6(a)–6(c) show the sensor response with f_H values of 1, 0.5, and 0.1 Hz, respectively. The orange solid line is the simulated field as a function of time based on the set frequency and amplitude. The black triangles are measured output voltages. A phase offset is added to the simulated field curve. As can be seen, measured V_{out} varies synchronously with the simulated field, indicating that the sensor can also be used to detect an ac field.

D. Effect of the out-of-plane field component on sensor performance

Finally, it is worth commenting on the effect of the vertical field component (H_z), as it can also induce magnetization switching, in addition to the DL SOT field. The presence of any finite H_z would result in the magnetization

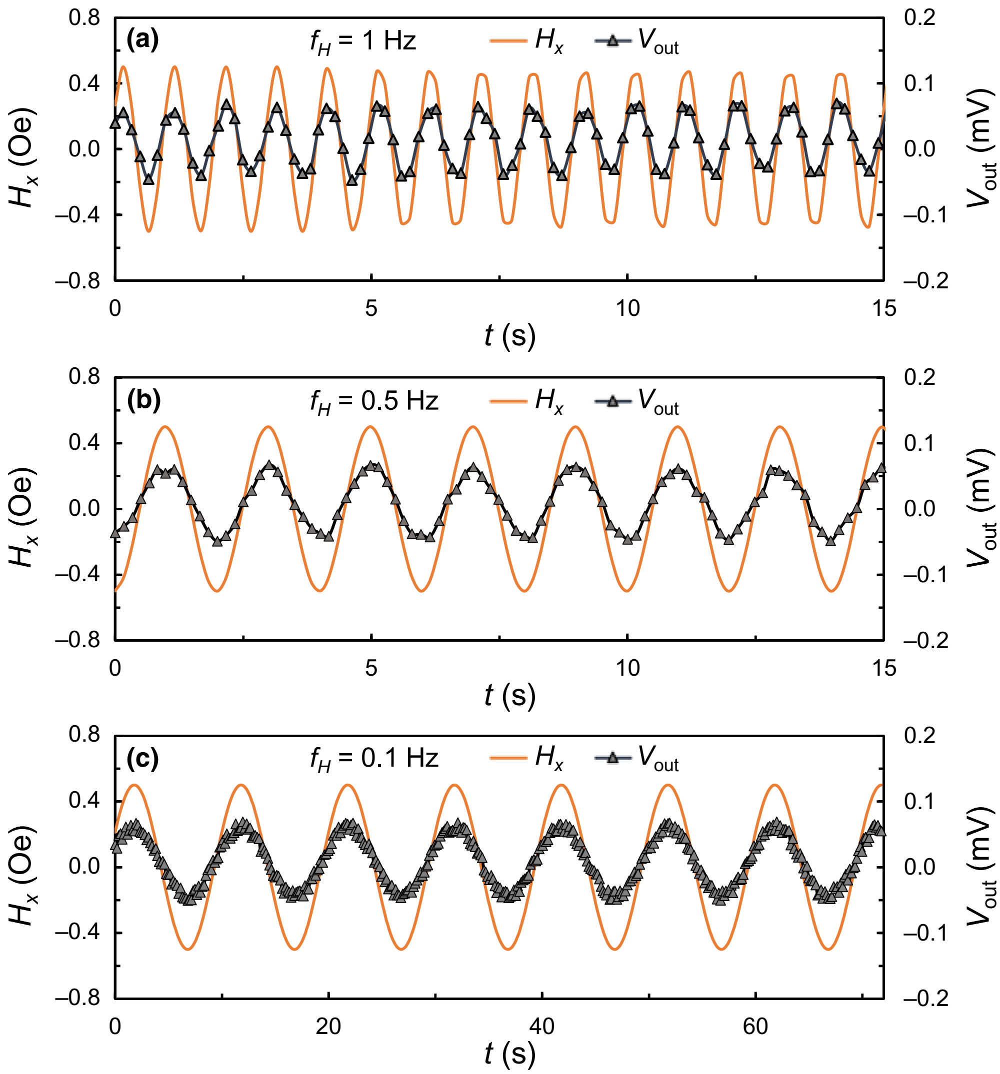

FIG. 6. (a)–(c) V_{out} and H_x as a function of time with ac field frequencies, f_H, of 1, 0.5, and 0.1 Hz, respectively.

staying in the H_z direction longer than that in the opposite direction for a periodic driving current, which seems to indicate that it will cause asymmetry in the signal response. However, this is actually not true because the average signal caused by H_z will be zero as the current changes its polarity periodically. Therefore, the main effect of H_z will be on the sensor's output voltage, rather than symmetry or cross-interference between H_x and H_z.

We examine the angular dependence of the sensor performance for both case 2 and case 3. Figures 7(a) and 7(d) show the output voltage of the sensor as a function of field polar angle, θ_H, with a fixed applied field at 160 K (case 2) and 300 K (case 3), respectively. Here, θ_H values of 90° and 270° correspond to the directions along $+x$ and $-x$, respectively. As can be seen, the sensor output amplitude has a strong dependence on θ_H. At 160 K, the sensor output exhibits a broad minimum at around $\theta_H = 0°$ and 180° and a broad maximum around $\theta_H = 90°$ and 270°, which is expected from its working principle. The former is due to the alignment of magnetization along the $+z$ and $-z$ directions, respectively, whereas the latter results from the hysteresis of the switching loop. In addition, we also notice dips at 90° and 270°, which might be caused by the multiple domains induced by the field when it is applied initially along the z direction. At 300 K, the angle dependence of the output voltage is simpler without the plateaus at around 90° and 270° due to the absence of a hysteresis, which can be well fitted by adding a z-component field to Eq. (6), as shown in the inset of Fig. 7(d).

We further test the sensor response to the applied field, H_θ, with different polar angles. From Figs. 7(b) and 7(c), we can see that the output amplitude at θ_H values of 70° and 110° is comparable and even slightly larger than that at $\theta_H = 90°$ shown in Fig. 3(a). However, the linearity range decreases. Further increasing the angle deviation from 90° ($<70°$ or $>110°$) will result in an evident reduction in the output voltage and linearity. On the other hand, for the 300 K case, as can be seen from Figs. 7(e) and 7(f), both the output amplitude and linearity range constantly decrease as the angle deviates away from $\theta_H = 90°$. Although one may

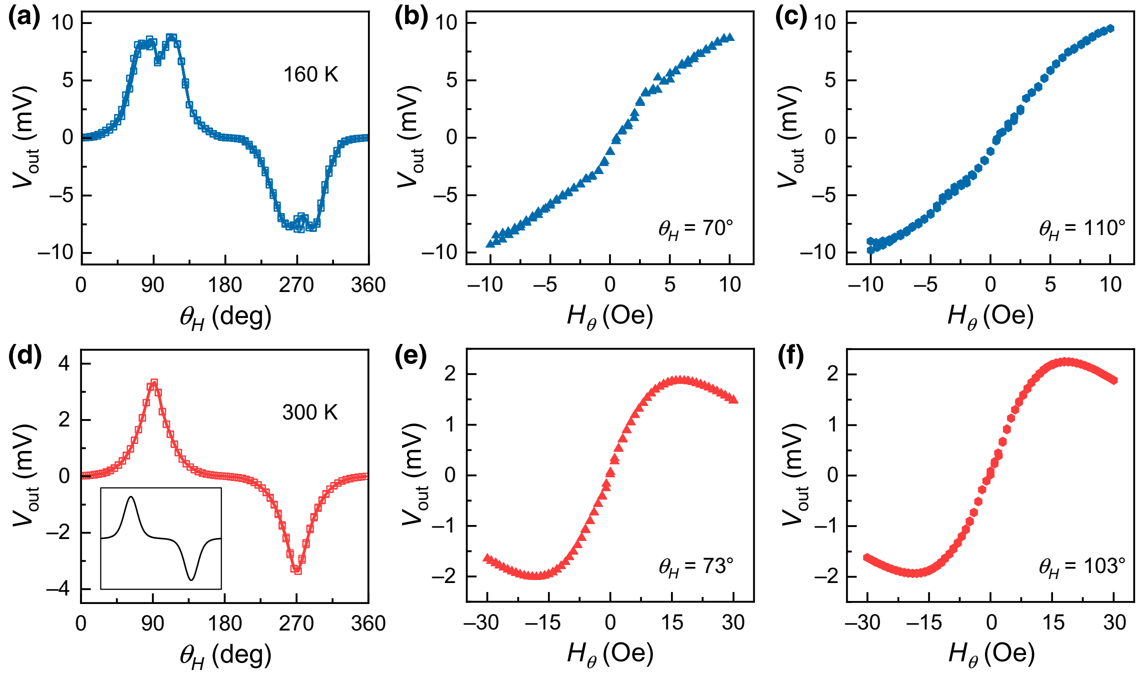

FIG. 7. (a) V_{out} of the STG sensor as a function of field polar angle, θ_H, with a fixed applied field of 8 Oe at 160 K. (b),(c) V_{out} in response to H_θ swept forth and back between −10 and 10 Oe at 160 K, with θ_H values of 70° and 110°, respectively. (d) V_{out} as a function of θ_H with a fixed applied field of 20 Oe at 300 K. Inset, simulated V_{out} as a function of θ_H. (e),(f) V_{out} in response to H_θ swept forth and back between −30 and 30 Oe at 300 K, with θ_H values of 73° and 103°, respectively.

consider this to be one of the limitations of the STG sensor, it can also be advantageous in applications that require a good field directionality of the sensor.

E. Proof-of-concept application of the STG sensor in angle detection

Due to its simple structure, good linearity, and negligible offset and hysteresis, the STG sensor is expected to have many potential applications. As one of the proof-of-concept experiments, here we demonstrate its application in position sensing. To this end, we apply a rotational field of 20 Oe in the x-y plane and measure the output of the sensor using the same procedure as that described above for every 5° of rotation. Figure 8(a) shows the output voltages, V_{out1} and V_{out2}, of the sensor with the longitudinal directions placed along the x direction and y direction, respectively, as a function of the external field angle φ_H. The sensor is driven by a square wave with an amplitude of 2 mA and frequency of 115 Hz. As can be seen, V_{out1} and V_{out2} have cosine and sine dependences on the field angle, which can be well fitted by $V_1 \cos\varphi_H$ and $V_2 \sin\varphi_H$, respectively, where V_1 and V_2 are the amplitudes of V_{out1} and V_{out2}, respectively. The field angle φ can be calculated from

$$\varphi = \text{acrtan2}\left[-\frac{V_{\text{out2}}}{V_2}, -\frac{V_{\text{out1}}}{V_1}\right] + \pi, \tag{7}$$

which is equivalent to $\varphi = \text{acrtan2}[-\sin\varphi, -\cos\varphi] + \pi$. Since the arctan $2[\sin\varphi, \cos\varphi]$ function gives the angle φ in the range from −180° to 180°, we add a phase shift

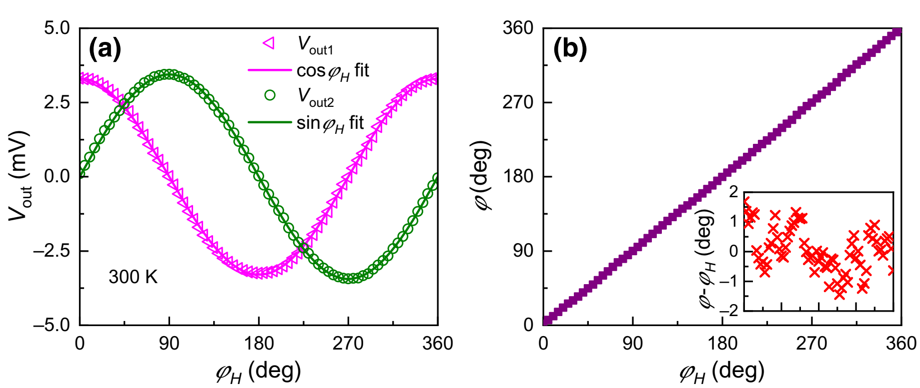

FIG. 8. (a) Output voltage of the Hall device with $\varphi_H = 0°$ aligned along x and y directions and a field of 20 Oe is rotated in the film plane. (b) Measured rotational angle φ as a function of φ_H. Inset, angle error $\varphi - \varphi_H$ in the full range of 360°.

π and a vertical shift π in the function to map the angle in the range between 0° and 360°. The detected angle φ from Eq. (7) is shown in Fig. 8(b) versus the actual field angle φ_H, from which a very linear relationship of φ and φ_H is observed. The calculated angle error $(\varphi - \varphi_H)$ at each position is shown in the inset of Fig. 8(b). As can be seen, the angle error is mostly within 1°, except for a few positions, with average and maximum values of 0.59° and 1.68°, respectively, indicating the accurate angle detection ability of the STG magnetic sensor. Unlike magnetoresistance sensors, which require an additional Hall sensor to differentiate angles between 0–180° and 180–360° due to the quadratic dependence on the field angle, here we need only two STG sensors to resolve a full rotation of 360°. Compared with the SOT-enabled angular position sensor that senses the second-harmonic Hall voltage reported in our previous work [65], the output voltage of the STG sensor is more than one order of magnitude larger, and it also does not suffer from dc offset and influence from the planar Hall effect.

IV. CONCLUSIONS

We propose and demonstrate a spin torque gate magnetic sensor that utilizes the longitudinal field dependence of current-induced magnetization switching in FM/HM bilayers. Driven by an ac current, and with the Hall voltage averaged over a large number of cycles, the sensor exhibits a linear response to the external magnetic field with a negligible hysteresis and dc offset. As a proof-of-concept demonstration, we implement the STG sensor on the Hall bar device with WTe_2/Ti/(Co, Fe)B stacks, where sputtering-deposited WTe_2 is employed as the SOT generator due to its large spin Hall angle. The temperature-dependence of PMA in WTe_2/Ti/(Co, Fe)B allows us to demonstrate the STG sensor in both DW-driven and stochastic magnetization reversal regimes. Despite the unoptimized structure, the sensor already shows a comparable sensitivity to and a much larger dynamic range than the SMR sensor demonstrated by us recently, which is also enabled by the SOT effect. The extremely simple structure of the STG sensor makes it attractive for many potential applications, as manifested in our proof-of-principle experiments in angle detection.

ACKNOWLEDGMENTS

This project is supported by the Ministry of Education, Singapore, under its Tier 2 Grants (Grants No. MOE2018-T2-1-076 and No. MOE2017-T2-2-011).

APPENDIX A: DERIVATION OF OUTPUT VOLTAGE WITH DIFFERENT ac WAVEFORMS

1. Sine wave

Figure 9 shows a sinusoidal ac current together with the Hall resistance R_H when $H_x > 0$, which can be expressed mathematically as

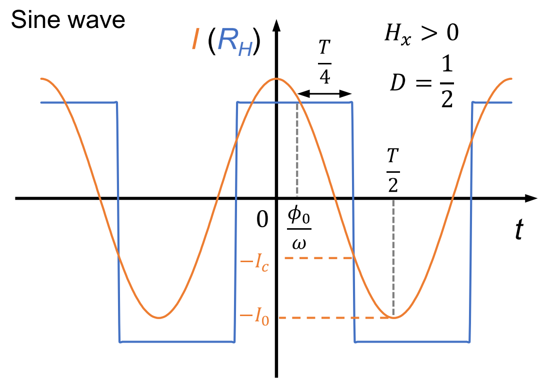

FIG. 9. The ac current I (sine wave) and Hall resistance R_H as a function of time, when $H_x > 0$.

$$I(t) = I_0 \cos \omega t, \tag{A1}$$

$$R_H(t) = R_0 + \mathrm{sgn}(H_x)\left[R_{\mathrm{AHE}}(2D-1) + \sum_{n=1}^{+\infty} \frac{4R_{\mathrm{AHE}}}{n\pi} \sin n\pi D \cos n(\omega t - \phi_0)\right], \tag{A2}$$

where we assume that the current amplitude I_0 is larger than the critical current I_c; ω is the angular frequency; ϕ_0 is the phase shift of $R_H(t)$ with respect to $t = 0$; D is the duty ratio of $R_H(t)$; R_0 is the offset resistance induced by misalignment of Hall voltage electrodes; and $\mathrm{sgn}(H_x)$ represents the switching polarity, which depends on the direction of H_x. For the sine wave, D is 50%. Therefore, $R_H(t)$ is reduced to $R_H(t) = R_0 + \mathrm{sgn}(H_x) \sum_{n=1}^{+\infty} \frac{4R_{\mathrm{AHE}}}{n\pi} \sin \frac{n\pi}{2} \cos n(\omega t - \phi_0)$. We can then write the Hall voltage, $V_H(t)$, as

$$V_H(t) = I(t)R_H(t) = I_0 \cos \omega t \left[R_0 + \mathrm{sgn}(H_x) \times \sum_{n=1}^{+\infty} \frac{4R_{\mathrm{AHE}}}{n\pi} \sin \frac{n\pi}{2} \cos n(\omega t - \phi_0)\right]. \tag{A3}$$

The output voltage V_{out}, obtained by averaging $V_H(t)$ over multiple cycles, is given by

$$V_{\mathrm{out}} = \frac{1}{T}\int_0^T V_H(t)dt = \frac{4I_0R_{\mathrm{AHE}}}{\pi T}\mathrm{sgn}(H_x) \times \int_0^T \sum_{n=1}^{+\infty} \cos \omega t \frac{\cos n(\omega t - \phi_0) \sin(n\pi/2)}{n} dt. \tag{A4}$$

It is worth noting that, mathematically, averaging over many cycles is equivalent to averaging over one cycle, but, in an actual sensing operation, averaging over many cycles contributes to noise reduction. By using the orthogonality property of sine and cosine functions, Eq. (A4) can be reduced to

$$V_{\text{out}} = \frac{2I_0R_{\text{AHE}}}{\pi}\text{sgn}(H_x)\cos\phi_0. \tag{A5}$$

Since $I[(T/4)+(\phi_0/\omega)] = -I_c$ (as can be seen from Fig. 9), $I_0\cos[\omega(T/4)+\phi_0] = -I_c$, we can obtain $\cos\phi_0 = \sqrt{1-[(I_c/I_0)]^2}(I_0 \geq I_c)$. Substituting the critical current [35] $I_c = (2e/\hbar)(M_s t_{\text{FM}} S/\theta_{\text{SH}})\left[(H_k^{\text{eff}}/2) - \left(|H_x|/\sqrt{2}\right)\right]$ $(H_k^{\text{eff}} \gg H_x)$ into $\cos\phi_0$ in Eq. (A5), we can obtain

$$V_{\text{out}} = \text{sgn}(H_x)\frac{2R_{\text{AHE}}}{\pi}\sqrt{I_0^2 - k^2\left(\frac{H_k^{\text{eff}}}{2} - \frac{|H_x|}{\sqrt{2}}\right)^2}, \tag{A6}$$

where $k = (2e/\hbar)(M_s t_{\text{FM}} S/\theta_{\text{SH}})$. When $I_0 = k(H_k^{\text{eff}}/2)$ and H_x is small, V_{out} can be written as

$$V_{\text{out}} = \text{sgn}(H_x)\frac{\sqrt{2}R_{\text{AHE}}k}{\pi}\sqrt{\sqrt{2}H_k^{\text{eff}}|H_x|}. \tag{A7}$$

Therefore, the output voltage has a nonlinear relationship with the longitudinal field in the sine-wave case, which cannot be used as a linear sensor.

2. Sawtooth wave

Next, we examine the case of an ac current with a sawtooth waveform, as shown in Fig. 10. In this case, the current and Hall resistance are given by

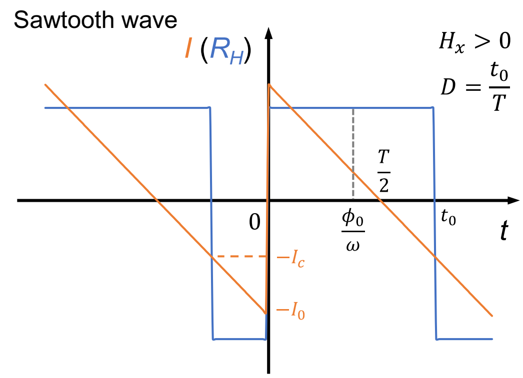

FIG. 10. The ac current I (sawtooth wave) and Hall resistance R_H as a function of time, when $H_x > 0$.

$$I(t) = \sum_{n=1}^{\infty}\frac{2I_0}{n\pi}\sin n\omega t, \tag{A8}$$

$$R_H(t) = R_0 + \text{sgn}(H_x)\left[R_{\text{AHE}}(2D-1) + \sum_{m=1}^{+\infty}\frac{4R_{\text{AHE}}}{m\pi}\sin m\pi D\cos m(\omega t - \phi_0)\right]. \tag{A9}$$

The Hall voltage, $V_H(t)$, can be then written as

$$V_H(t) = \left\{R_0 + \text{sgn}(H_x)\left[R_{\text{AHE}}(2D-1) + \sum_{m=1}^{+\infty}\frac{4R_{\text{AHE}}}{m\pi}\sin m\pi D\cos m(\omega t - \phi_0)\right]\right\}\sum_{n=1}^{\infty}\frac{2I_0}{n\pi}\sin n\omega t, \tag{A10}$$

which leads to the averaged output of

$$V_{\text{out}} = \frac{1}{T}\int_0^T V_H(t)dt = \frac{2R_{\text{AHE}}I_0\text{sgn}(H_x)}{T}\int_{m=1}^{T}\frac{4}{m\pi}\sin m\pi D\cos m(\omega t - \phi_0)\sum_{n=1}^{\infty}\frac{1}{n\pi}\sin n\omega t dt, \tag{A11}$$

where the $R_0\sum_{n=1}^{\infty}(2I_0/n\pi)\sin n\omega t$ and $\text{sgn}(H_x)R_{\text{AHE}}(2D-1)\sum_{n=1}^{\infty}(2I_0/n\pi)\sin n\omega t$ terms in $V_H(t)$ are averaged to zero. Equation (A11) can be further reduced to

$$\begin{aligned}
V_{\text{out}} &= \frac{8a}{\pi^2 T}\left[\int_0^T\sum_{m=1}^{+\infty}\sum_{n=1}^{\infty}\frac{1}{mn}\sin m\pi D\cos m(\omega t - \phi_0)\sin n\omega t dt\right] \\
&= \frac{8a}{\pi^2 T}\left(\int_0^T\sum_{m=1}^{+\infty}\sum_{n=1}^{\infty}\frac{1}{2mn}\sin m\pi D\{\sin[(m+n)\omega t - m\phi_0] - \sin[(m-n)\omega t - m\phi_0]\}\right) \\
&= \frac{4a}{\pi^2}\sum_{n=m=1}^{+\infty}\frac{1}{nm}\sin m\pi D\sin m\phi_0,
\end{aligned} \tag{A12}$$

where $a = R_{\rm AHE} I_0 {\rm sgn}(H_x)$, $D = (t_0/T) = [(I_c + I_0)/(2I_0)]$, and $(\phi_0/\omega) = (t_0/2)$. Therefore, we have

$$V_{\rm out} = \frac{a}{\pi^2}\sum_{n=1}^{+\infty}\frac{1}{n^2}\sin^2 n\pi\left(\frac{I_c+I_0}{2I_0}\right) = \frac{2a}{\pi^2}\sum_{n=1}^{+\infty}\frac{1}{n^2}\left[1-\cos^2 n\pi\left(\frac{I_c+I_0}{2I_0}\right)\right] = \frac{2a}{\pi^2}\sum_{n=1}^{+\infty}\frac{1}{n^2}\left(1-\cos n\pi\cos n\pi\frac{I_c}{I_0}\right)$$
$$= \frac{2a}{\pi^2}\left\{\sum_{n=1}^{+\infty}\frac{1}{n^2} - \sum_{n=1}^{+\infty}\frac{1}{n^2}\left[\cos n\left(\pi-\frac{I_c}{I_0}\pi\right)+\cos n\left(\pi+\frac{I_c}{I_0}\pi\right)\right]\right\}. \tag{A13}$$

Since $\sum_{n=1}^{+\infty}(1/n^2) = (\pi^2/6)$ and $\sum_{n=1}^{+\infty}(1/n^2)\cos nx = (x^2/4) - (\pi x/2) + (\pi^2/6)$, we can obtain

$$V_{\rm out} = \frac{a}{\pi^2}\left\{\frac{\pi^2}{3} - \frac{\left[\pi-\left(\frac{I_c}{I_0}\right)\pi\right]^2}{4} + \frac{\pi\left[\pi-\left(\frac{I_c}{I_0}\right)\pi\right]}{2} - \frac{\pi^2}{6} - \frac{\left[\pi+\left(\frac{I_c}{I_0}\right)\pi\right]^2}{4} + \frac{\pi\left[\pi+\left(\frac{I_c}{I_0}\right)\pi\right]}{2} - \frac{\pi^2}{6}\right\}$$
$$= \frac{a}{2\pi^2}\left[\pi^2 - \left(\frac{I_c}{I_0}\pi\right)^2\right] = R_{\rm AHE}sgn(H_x)\frac{I_0^2 - I_c^2}{2I_0}, \tag{A14}$$

which can be further expressed as a function of H_x:

$$V_{\rm out} = R_{\rm AHE}sgn(H_x)\frac{I_0^2 - k^2\left[(H_k^{\rm eff}/2) - \left(|H_x|/\sqrt{2}\right)\right]^2}{2I_0}. \tag{A15}$$

When $I_0 = k(H_k^{\rm eff}/2)$, the output will be

$$V_{\rm out} = \frac{R_{\rm AHE}k}{\sqrt{2}}H_x. \tag{A16}$$

Therefore, we obtain a linear response to the longitudinal field, and, importantly, the offset due to misalignment of electrodes, if any, is automatically suppressed due to the SOT gating operation.

3. Triangle wave

We now consider a more commonly used ramp wave, a triangle wave. The current and Hall resistance for the triangle wave are shown in Fig. 11, which can be expressed as

$$I(t) = \sum_{n=1}^{\infty}\frac{8I_0}{n^2\pi^2}\cos n\omega t, \tag{A17}$$

$$R_H(t) = R_0 + {\rm sgn}(H_x)\sum_{m=1}^{+\infty}\frac{4R_{\rm AHE}}{m\pi}\sin\frac{m\pi}{2}\cos m(\omega t - \phi_0). \tag{A18}$$

The Hall voltage, $V_H(t)$, is then given by

$$V_H(t) = \left[R_0 + {\rm sgn}(H_x)\sum_{m=1}^{+\infty}\frac{4R_{\rm AHE}}{m\pi}\sin\frac{m\pi}{2} \times \cos m(\omega t-\phi_0)\right]\sum_{n=1}^{\infty}\frac{8I_0}{n^2\pi^2}\cos n\omega t, \tag{A19}$$

from which the output voltage is derived as

$$V_{\rm out} = \frac{1}{T}\int_0^T V_H(t)dt = \frac{32a}{T}\left[\int_0^T\sum_{m=1}^{+\infty}\frac{1}{m\pi}\sin\frac{m\pi}{2}\cos m(\omega t-\phi_0)\sum_{n=1}^{\infty}\frac{1}{n^2\pi^2}\cos n\omega t dt\right]$$
$$= \frac{32a}{\pi^3 T}\left[\int_0^T\sum_{m=1}^{+\infty}\sum_{n=1}^{\infty}\frac{1}{2mn^2}\sin\frac{m\pi}{2}\{\cos[(m+n)\omega t - m\phi_0] + \cos[(m-n)\omega t - m\phi_0]\}dt\right] \tag{A20}$$
$$= \frac{16a}{\pi^3}\sum_{n=m=1}^{+\infty}\frac{1}{mn^2}\sin\frac{m\pi}{2}\cos m\phi_0,$$

where $a = R_{\rm AHE} I_0 {\rm sgn}(H_x)$ and ϕ_0 can be obtained from the relation $[\{[(\phi_0/\omega) + (T/4)]/(T/2)\} = (I_c + I_0)/(4I_0)]$ as $\phi_0 = (I_c/2I_0)\pi$. Therefore, $V_{\rm out}$ can be further written as

$$
\begin{aligned}
V_{\text{out}} &= \frac{16a}{\pi^3}\sum_{n=1}^{+\infty}\frac{1}{n^3}\sin\frac{n\pi}{2}\cos n\pi\left(\frac{I_c}{2I_0}\right) = \frac{8a}{\pi^3}\sum_{n=1}^{+\infty}\frac{1}{n^3}\left\{\sin\frac{n[\pi+(I_c/I_0)\pi]}{2}+\sin\frac{n[\pi-(I_c/I_0)\pi]}{2}\right\}\\
&= \frac{8a}{\pi^3}\sum_{n=1}^{+\infty}\frac{1}{n^3}\left(\sin\frac{n[\pi+(I_c/I_0)\pi]}{2}-\sin\left\{\frac{n[\pi+(I_c/I_0)\pi]}{2}-n\pi\right\}\right)\\
&= \frac{8a}{\pi^3}\sum_{n=1}^{+\infty}\frac{1}{n^3}[1-(-1)^n]\sin\frac{n[\pi+(I_c/I_0)\pi]}{2}.
\end{aligned}
\tag{A21}
$$

According to the sine series of x^2 and x,

$$
x^2 = \frac{2}{\pi}\sum_{n=1}^{+\infty}\left\{\frac{2}{n^3}[(-1)^n-1]\sin nx-(-1)^n\pi^2\frac{\sin nx}{n}\right\},
$$

and $x = 2\sum_{n=1}^{+\infty}(-1)^{n+1}(\sin nx/n)$, we can reduce V_{out} to

$$
V_{\text{out}} = \frac{8a}{\pi^3}\left\{-\frac{\pi}{4}\left[\frac{\pi+(I_c/I_0)\pi}{2}\right]^2+\frac{\pi^2}{4}\frac{[\pi+(I_c/I_0)\pi]}{2}\right\} = \frac{a}{2\pi^3}\left[\pi^3-\pi\left(\frac{I_c}{I_0}\pi\right)^2\right] = R_{\text{AHE}}sgn(H_x)\frac{I_0^2-I_c^2}{2I_0}. \tag{A22}
$$

As can be seen, V_{out} has the same expression as that for the sawtooth wave. When $I_0 = k(H_k^{\text{eff}}/2)$, the output voltage will be $V_{\text{out}} = (R_{\text{AHE}}k/\sqrt{2})H_x$, which is linear with respect to the longitudinal field. Again, the offset due to electrode misalignment is suppressed.

4. Square wave

Finally, we consider the case of a square wave, as shown in Figs. 12(a) and 12(b). In this case, $R_H(t)$ and $V_H(t)$ also have a square waveform with the same duty ratio and zero phase difference with $I(t)$. This results in a constant amplitude of output voltage at different H_x, as shown in Fig. 12(c), which can be expressed as $V_{\text{out}} = \text{sgn}(H_x)I_0R_{\text{AHE}}$. Therefore, in this case, the device does not function as a sensor, as it can only detect the direction of the external field.

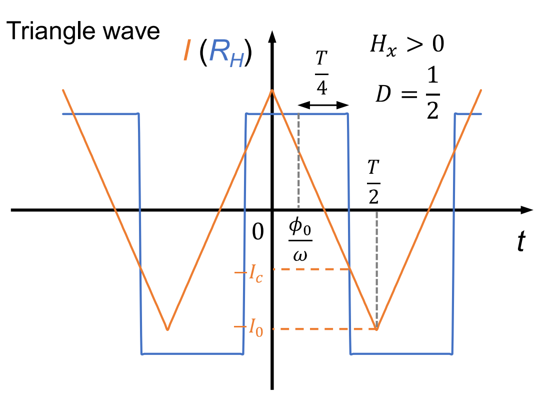

FIG. 11. The ac current I (triangle wave) and Hall resistance R_H as a function of time, when $H_x > 0$.

APPENDIX B: DERIVATION OF OUTPUT VOLTAGE FOR STG SENSOR WITH HYPERBOLIC TANGENT SWITCHING BEHAVIOR

1. Sine wave

When the sensor is driven by a sine wave, the Hall voltage is $V_H(t) = I_0\sin\omega t(R_0+R_H)$, where R_H can be expressed as a hyperbolic tangent function $R_H = R_0 + R_{\text{AHE}}\tanh(M_sH_zV/k_BT)$. When H_z is derived from the DL SOT effective field, we have $H_z^{\text{DL}} = H^{\text{DL}}m_x$. Therefore, to create an effective field in the z direction, a longitudinal field is required to orient the magnetization of the element in the x direction. When H_x is small, we may assume that $H_z^{\text{DL}} = (H^{\text{DL}}/H_k^{\text{eff}})H_x$, with $H^{\text{DL}} = (\hbar/2e)(\theta_{\text{SH}}/M_st_{\text{FM}}S)I_0\sin\omega t$. From the above relationship, we can obtain the Hall voltage in the small field range as

$$
V_H(t) = I_0\sin\omega tR_0 + I_0\sin\omega tR_{\text{AHE}}\tanh \times\left(I_0\sin\omega t\frac{M_sV}{k_BT}\frac{\hbar}{2e}\frac{\theta_{\text{SH}}}{M_st_{\text{FM}}S}\frac{H_x}{H_k^{\text{eff}}}\right). \tag{B1}
$$

At small H_x, Eq. (B1) can be reduced to

$$
V_H(t) = I_0\sin\omega tR_0 + (I_0\sin\omega t)^2R_{\text{AHE}}\frac{1}{k_BT}\frac{\hbar}{2e}\frac{\theta_{\text{SH}}}{H_k^{\text{eff}}}H_x, \tag{B2}
$$

By averaging the voltage over one cycle, we can obtain the output voltage as

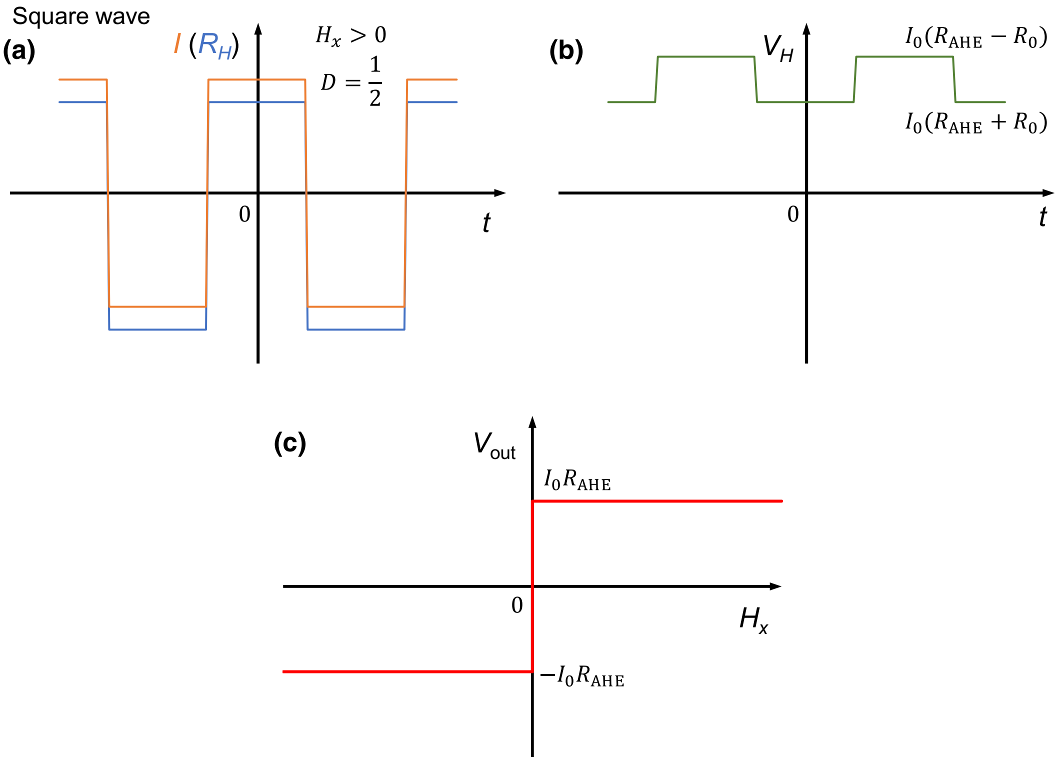

FIG. 12. (a),(b) The ac current I, Hall resistance R_H, and Hall voltage V_H as a function of time in the case of a square wave, when $H_x > 0$. (c) Output voltage $V_{\rm out}$ as a function of in-plane field H_x.

$$V_{\rm out} = \frac{1}{T'}\int_0^{T'} V_H dt = I_0^2 R_{\rm AHE}\frac{1}{k_B T T'}\frac{\hbar}{2e}\frac{\theta_{\rm SH}}{H_k^{\rm eff}} H_x \int_0^{T'} sin^2 \omega t dt$$
$$= \frac{I_0^2 R_{\rm AHE}}{2}\frac{1}{k_B T}\frac{\hbar}{2e}\frac{\theta_{\rm SH}}{H_k^{\rm eff}} H_x = \frac{1}{2} I_0^2 R_{\rm AHE} b H_x. \tag{B3}$$

where $b = (1/k_B T)(\hbar/2e)(\theta_{\rm SH}/H_k^{\rm eff})$, the cycle period here is written as T' to differentiate from temperature T. As can be seen, $V_{\rm out}$ is linear with respect to H_x at small field.

2. Square wave

Similarly, when the sensor is driven by a square wave (duty cycle of 50%), by changing the current expression from $I_0 \sin\omega t$ to $\sum_{n=1}^{+\infty}(4I_0/n\pi)\sin(n\pi/2)\cos n\omega t$, we can write

$$V_H(t) = R_0 \sum_{n=1}^{+\infty}\frac{4I_0}{n\pi}\sin\frac{n\pi}{2}\cos n\omega t + bR_{\rm AHE}H_x \sum_{n=1}^{+\infty}\left(\frac{4I_0}{n\pi}\sin\frac{n\pi}{2}\cos n\omega t\right)^2, \tag{B4}$$

which leads to an output voltage of

$$V_{\rm out} = \frac{1}{T'}\int_0^{T'} V_H dt = (16 I_0^2 R_{\rm AHE} b/\pi^2 T')H_x \times \int_0^{T'}\sum_{n=1}^{+\infty}\left(\frac{1}{n}\sin\frac{n\pi}{2}\cos n\omega t\right)^2 dt$$
$$= \frac{16 I_0^2 R_{AHE} b}{\pi^2 T'} H_x \int_0^{T'}\frac{1}{n^2}\frac{(1-\cos n\pi)(1+\cos 2n\omega t)}{4} dt$$
$$= \frac{4 I_0^2 R_{AHE} b}{\pi^2 T'} H_x \int_0^{T'}\sum_{n=1}^{+\infty}\frac{1}{n^2}[1-(-1)^n] dt$$
$$= I_0^2 R_{AHE} b H_x. \tag{B5}$$

Therefore, a linear response to H_x can also be achieved when the sensor is driven by a square wave. The amplitude of $V_{\rm out}$ is twice that of the sine wave case, which is consistent with the experimental results as shown in Fig. 13.

3. Sawtooth wave

For a sawtooth wave with $I = \sum_{n=1}^{+\infty}(2I_0/n\pi)\sin n\omega t$, we can obtain $V_{\rm out}$ as

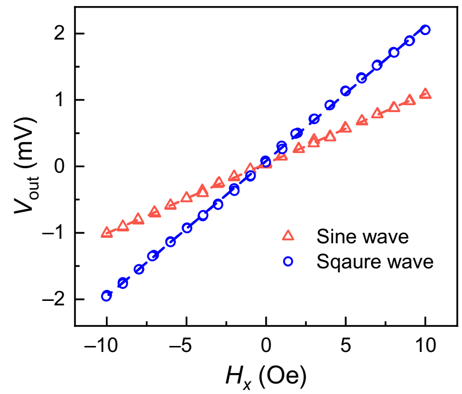

FIG. 13. Experimentally obtained V_{out} as a function of H_x swept forth and back between −10 and 10 Oe, when the sensor is driven by a square wave (squares) and sine wave (triangles).

$$V_{out} = \frac{4I_0^2 R_{AHE} b}{\pi^2 T'} H_x \int_0^{T'} \sum_{n=1}^{+\infty} \left(\frac{1}{n}\sin n\omega t\right)^2 dt$$
$$= \frac{2I_0^2 R_{AHE} b}{\pi^2 T'} H_x \int_0^{T'} \sum_{n=1}^{+\infty} \frac{1}{n^2} dt = \frac{1}{3} I_0^2 R_{AHE} b H_x. \quad (B6)$$

4. Triangle wave

For a triangle wave with $I = \sum_{n=1}^{+\infty} (8I_0/n^2\pi^2)\cos n\omega t$, the output voltage is

$$V_{out} = \frac{64 I_0^2 R_{AHE} b}{\pi^4 T'} H_x \int_0^{T'} \sum_{n=1}^{+\infty} \left(\frac{1}{n^2}\cos n\omega t\right)^2 dt$$
$$= \frac{32 I_0^2 R_{AHE} b}{\pi^4 T'} H_x \int_0^{T'} \sum_{n=1}^{+\infty} \frac{1}{n^4} dt$$
$$= \frac{16}{45} I_0^2 R_{AHE} b H_x. \quad (B7)$$

Therefore, we show that a linear sensor can be obtained by using all different types of current waveforms.

APPENDIX C: RESPONSE OF THE STG SENSOR WITH SMALLER FIELD STEPS

The results of sensor response shown in Figs. 3 and 4 are measured on the VersaLab PPMS system, in which field steps below 0.5 Oe are difficult to achieve. The sensor can detect a lower field because switching will still occur with even a very small in-plane assisting field, when the applied current is sufficiently large. This small field will increase the probability of switching towards one direction, leading to nonzero sensor output. Experimentally, we try to measure the sensor response with a smaller field step. Figure 14(a) shows V_{out} as a function of H_x at 160 K, with the field step set to 0.1 Oe. As can be seen, although the actual field step is not constantly 0.1 Oe (due to equipment accuracy), the linearity error [shown in the inset of Fig. 14(a)] is mostly within 5%, except for few points. For case 3, due to the superparamagnetic property, the minimum field that can be detected by the sensor should be much smaller than that of case 2. Therefore, we measure the sensor response in a Helmholtz coil, which allows a field step as small as nT. Figure 14(b) and the inset show V_{out} and the linearity error as a function of H_x at 300 K with a field step of 0.02 Oe and the sensor current frequency is set to 10 015 Hz, from which the maximum linearity error is 4.1%. A further decrease in the field step will result in a linearity error larger than 5%. Therefore, if one is mainly concerned with the linearity of the sensor, the minimum field that can be detected by this particular sensor is around 0.02 Oe. This is certainly not the minimum detectable field of the STG sensor.

The field resolution of the sensor can be further improved by averaging more cycles by increasing the sampling duration or employing a DAQ device with a higher sampling rate. Since we have not completed the experimental setup for the noise-spectrum analysis of the STG sensor yet, here, we estimate the detectivity of the STG sensor to be 300 K based on the $1/f$ magnetic noise. The power density of $1/f$ noise is given by $S_V = (\delta_H V_b^2/N_c V_{eff} f)$, where δ_H is the Hooge constant, V_b is the voltage across the Hall cross area, N_c is the free-electron density, V_{eff} is the effective volume of the FM layer, and

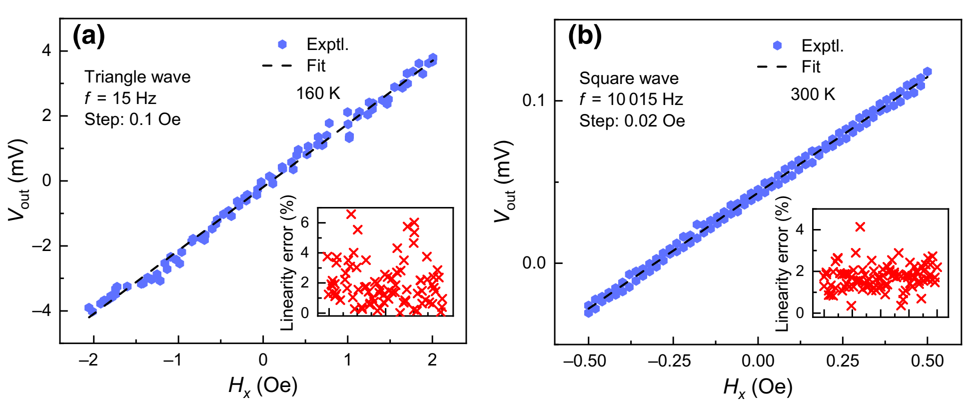

FIG. 14. (a) V_{out} in response to H_x swept forth and back between −2 and 2 Oe at 160 K with field step of 0.1 Oe. Sensor is driven by an ac current with triangle waveform and frequency of 15 Hz. (b) V_{out} in response to H_x swept forth and back between −0.5 and 0.5 Oe at 300 K with field step of 0.02 Oe. Sensor is driven by an ac current with square waveform and frequency of 10 015 Hz. Insets, linearity error at each field.

f is the frequency [66,67]. By using a Hooge constant of $\delta_H = 0.002$, as obtained for the SMR sensor driven by ac current in our previous work [32], and substituting $V_b = 0.332$ V, $N_c = 1.7 \times 10^{29}$ m^{-3}, $V_{\text{eff}} = 1.125 \times 10^{-19}$ m^3, and $f = 10\,015$ Hz into the above equation, we estimate the detectivity of the STG sensor at 300 K to be around 0.92 nT/$\sqrt{\text{Hz}}$, which is at a similar level to that of the detectivity of the ac-excited SMR sensor at high frequency [32].

[1] I. M. Miron, K. Garello, G. Gaudin, P.-J. Zermatten, M. V. Costache, S. Auffret, S. Bandiera, B. Rodmacq, A. Schuhl, and P. Gambardella, Perpendicular switching of a single ferromagnetic layer induced by in-plane current injection, Nature **476**, 189 (2011).

[2] L. Liu, C.-F. Pai, Y. Li, H. W. Tseng, D. C. Ralph, and R. A. Buhrman, Spin-torque switching with the giant spin Hall effect of tantalum, Science **336**, 555 (2012).

[3] G. Yu, P. Upadhyaya, Y. Fan, J. G. Alzate, W. Jiang, K. L. Wong, S. Takei, S. A. Bender, L.-T. Chang, Y. Jiang, M. Lang, J. Tang, Y. Wang, Y. Tserkovnyak, P. K. Amiri, and K. L. Wang, Switching of perpendicular magnetization by spin–orbit torques in the absence of external magnetic fields, Nat. Nanotechnol. **9**, 548 (2014).

[4] S. Fukami, T. Anekawa, C. Zhang, and H. Ohno, A spin–orbit torque switching scheme with collinear magnetic easy axis and current configuration, Nat. Nanotechnol. **11**, 621 (2016).

[5] A. Manchon, J. Železný, I. M. Miron, T. Jungwirth, J. Sinova, A. Thiaville, K. Garello, and P. Gambardella, Current-induced spin-orbit torques in ferromagnetic and antiferromagnetic systems, Rev. Mod. Phys. **91**, 035004 (2019).

[6] Y. A. Bychkov and ÉI Rashba, Properties of a 2D electron gas with lifted spectral degeneracy, JETP Lett. **39**, 78 (1984).

[7] V. M. Edelstein, Spin polarization of conduction electrons induced by electric current in two-dimensional asymmetric electron systems, Solid State Commun. **73**, 233 (1990).

[8] M. I. D'Yakonov and V. I. Perel, Possibility of orienting electron spins with current, JETP Lett. **13**, 467 (1971).

[9] J. E. Hirsch, Spin Hall Effect, Phys. Rev. Lett. **83**, 1834 (1999).

[10] S. Zhang, Spin Hall Effect in the Presence of Spin Diffusion, Phys. Rev. Lett. **85**, 393 (2000).

[11] J. Sinova, S. O. Valenzuela, J. Wunderlich, C. H. Back, and T. Jungwirth, Spin Hall effects, Rev. Mod. Phys. **87**, 1213 (2015).

[12] A. Hoffmann, Spin Hall effects in metals, IEEE Trans. Magn. **49**, 5172 (2013).

[13] K. Garello, I. M. Miron, C. O. Avci, F. Freimuth, Y. Mokrousov, S. Blügel, S. Auffret, O. Boulle, G. Gaudin, and P. Gambardella, Symmetry and magnitude of spin–orbit torques in ferromagnetic heterostructures, Nat. Nanotechnol. **8**, 587 (2013).

[14] C. O. Avci, K. Garello, C. Nistor, S. Godey, B. Ballesteros, A. Mugarza, A. Barla, M. Valvidares, E. Pellegrin, A. Ghosh, I. M. Miron, O. Boulle, S. Auffret, G. Gaudin, and P. Gambardella, Fieldlike and antidamping spin-orbit torques in as-grown and annealed Ta/CoFeB/MgO layers, Phys. Rev. B **89**, 214419 (2014).

[15] M. Hayashi, J. Kim, M. Yamanouchi, and H. Ohno, Quantitative characterization of the spin-orbit torque using harmonic Hall voltage measurements, Phys. Rev. B **89**, 144425 (2014).

[16] L. Liu, O. J. Lee, T. J. Gudmundsen, D. C. Ralph, and R. A. Buhrman, Current-Induced Switching of Perpendicularly Magnetized Magnetic Layers Using Spin Torque From the Spin Hall Effect, Phys. Rev. Lett. **109**, 096602 (2012).

[17] Y.-C. Lau, D. Betto, K. Rode, J. M. D. Coey, and P. Stamenov, Spin–orbit torque switching without an external field using interlayer exchange coupling, Nat. Nanotechnol. **11**, 758 (2016).

[18] A. van den Brink, G. Vermijs, A. Solignac, J. Koo, J. T. Kohlhepp, H. J. Swagten, and B. Koopmans, Field-free magnetization reversal by spin-Hall effect and exchange bias, Nat. Commun. **7**, 10854 (2016).

[19] S. Fukami, C. Zhang, S. DuttaGupta, A. Kurenkov, and H. Ohno, Magnetization switching by spin–orbit torque in an antiferromagnet–ferromagnet bilayer system, Nat. Mater. **15**, 535 (2016).

[20] Y.-W. Oh, S.-h. Chris Baek, Y. M. Kim, H. Y. Lee, K.-D. Lee, C.-G. Yang, E.-S. Park, K.-S. Lee, K.-W. Kim, G. Go, J.-R. Jeong, B.-C. Min, H.-W. Lee, K.-J. Lee, and B.-G. Park, Field-free switching of perpendicular magnetization through spin–orbit torque in antiferromagnet/ferromagnet/oxide structures, Nat. Nanotechnol. **11**, 878 (2016).

[21] L. You, O. Lee, D. Bhowmik, D. Labanowski, J. Hong, J. Bokor, and S. Salahuddin, Switching of perpendicularly polarized nanomagnets with spin orbit torque without an external magnetic field by engineering a tilted anisotropy, Proc. Natl. Acad. Sci. U.S.A. **112**, 10310 (2015).

[22] J. Daughton, J. Brown, E. Chen, R. Beech, A. Pohm, and W. Kude, Magnetic field sensors using GMR multilayer, IEEE Trans. Magn. **30**, 4608 (1994).

[23] S. Parkin, J. Xin, C. Kaiser, A. Panchula, K. Roche, and M. Samant, Magnetically engineered spintronic sensors and memory, Proc. IEEE **91**, 661 (2003).

[24] Y. Wu, in *Encyclopedia of Nanoscience and Nanotechnology*, edited by H. S. Nalwa (American Scientific Publishers, Stevenson Ranch, 2003), Vol. 7, p. 493.

[25] J. Lenz and S. Edelstein, Magnetic sensors and their applications, IEEE Sens. J. **6**, 631 (2006).

[26] S. X. Wang and G. Li, Advances in giant magnetoresistance biosensors with magnetic nanoparticle tags: Review and outlook, IEEE Trans. Magn. **44**, 1687 (2008).

[27] C. Chappert, A. Fert, and F. N. Van Dau, The emergence of spin electronics in data storage, Nat. Mater. **6**, 813 (2007).

[28] P. Ripka and M. Janosek, Advances in magnetic field sensors, IEEE Sens. J. **10**, 1108 (2010).

[29] S. Tumanski, Modern magnetic field sensors–a review, Organ **10**, 1 (2013).

[30] Y. Yang, Y. Xu, H. Xie, B. Xu, and Y. Wu, Semitransparent anisotropic and spin Hall magnetoresistance sensor enabled by spin-orbit torque biasing, Appl. Phys. Lett. **111**, 032402 (2017).

[31] Y. Xu, Y. Yang, Z. Luo, B. Xu, and Y. Wu, Macrospin modeling and experimental study of spin-orbit torque biased magnetic sensors, J. Appl. Phys. **122**, 193904 (2017).

[32] Y. Xu, Y. Yang, M. Zhang, Z. Luo, and Y. Wu, Ultrathin all-in-one spin Hall magnetic sensor with built-in AC excitation enabled by spin current, Adv. Mater. Technol. **3**, 1800073 (2018).

[33] Y. Xu, Y. Yang, H. Xie, and Y. Wu, Spin Hall magnetoresistance sensor using Au_xPt_{1-x} as the spin-orbit torque biasing layer, Appl. Phys. Lett. **115**, 182406 (2019).

[34] Y. Xu, Y. Yang, and Y. Wu, Eddy current testing of metal cracks using spin Hall magnetoresistance sensor and machine learning, IEEE Sens. J. **20**, 10502 (2020).

[35] K.-S. Lee, S.-W. Lee, B.-C. Min, and K.-J. Lee, Threshold current for switching of a perpendicular magnetic layer induced by spin Hall effect, Appl. Phys. Lett. **102**, 112410 (2013).

[36] A. Kurenkov, C. Zhang, S. DuttaGupta, S. Fukami, and H. Ohno, Device-size dependence of field-free spin-orbit torque induced magnetization switching in antiferromagnet/ferromagnet structures, Appl. Phys. Lett. **110**, 092410 (2017).

[37] C. Zhang, S. Fukami, H. Sato, F. Matsukura, and H. Ohno, Spin-orbit torque induced magnetization switching in nanoscale Ta/CoFeB/MgO, Appl. Phys. Lett. **107**, 012401 (2015).

[38] S. Emori, U. Bauer, S.-M. Ahn, E. Martinez, and G. S. D. Beach, Current-driven dynamics of chiral ferromagnetic domain walls, Nat. Mater. **12**, 611 (2013).

[39] J. Feng, E. Grimaldi, C. O. Avci, M. Baumgartner, G. Cossu, A. Rossi, and P. Gambardella, Effects of Oxidation of Top and Bottom Interfaces on the Electric, Magnetic, and Spin-Orbit Torque Properties of $Pt/Co/AlO_x$ Trilayers, Phys. Rev. Appl. **13**, 044029 (2020).

[40] H. Xie, Z. Luo, Y. Yang, and Y. Wu, In situ study of oxygen and Mg effects on current-induced magnetization switching in Pt/Co bilayers in ultrahigh vacuum, Appl. Phys. Lett. **116**, 122404 (2020).

[41] O. J. Lee, L. Q. Liu, C. F. Pai, Y. Li, H. W. Tseng, P. G. Gowtham, J. P. Park, D. C. Ralph, and R. A. Buhrman, Central role of domain wall depinning for perpendicular magnetization switching driven by spin torque from the spin Hall effect, Phys. Rev. B **89**, 024418 (2014).

[42] J. Cao, Y. Chen, T. Jin, W. Gan, Y. Wang, Y. Zheng, H. Lv, S. Cardoso, D. Wei, and W. S. Lew, Spin orbit torques induced magnetization reversal through asymmetric domain wall propagation in Ta/CoFeB/MgO structures, Sci. Rep. **8**, 1355 (2018).

[43] S. Pizzini, J. Vogel, S. Rohart, L. D. Buda-Prejbeanu, E. Jué, O. Boulle, I. M. Miron, C. K. Safeer, S. Auffret, and G. Gaudin, Chirality-Induced Asymmetric Magnetic Nucleation in $Pt/Co/AlO_x$ Ultrathin Microstructures, Phys. Rev. Lett. **113**, 047203 (2014).

[44] N. Mikuszeit, O. Boulle, I. M. Miron, K. Garello, P. Gambardella, G. Gaudin, and L. D. Buda-Prejbeanu, Spin-orbit torque driven chiral magnetization reversal in ultrathin nanostructures, Phys. Rev. B **92**, 144424 (2015).

[45] G. Finocchio, M. Carpentieri, E. Martinez, and B. Azzerboni, Switching of a single ferromagnetic layer driven by spin Hall effect, Appl. Phys. Lett. **102**, 212410 (2013).

[46] M. Baumgartner, K. Garello, J. Mendil, C. O. Avci, E. Grimaldi, C. Murer, J. Feng, M. Gabureac, C. Stamm, Y. Acremann, S. Finizio, S. Wintz, J. Raabe, and P. Gambardella, Spatially and time-resolved magnetization dynamics driven by spin–orbit torques, Nat. Nanotechnol. **12**, 980 (2017).

[47] K. Y. Camsari, S. Salahuddin, and S. Datta, Implementing p-bits with embedded MTJ, IEEE Electron Device Lett. **38**, 1767 (2017).

[48] K. Y. Camsari, R. Faria, B. M. Sutton, and S. Datta, Stochastic p-Bits for Invertible Logic, Phys. Rev. X **7**, 031014 (2017).

[49] W. A. Borders, A. Z. Pervaiz, S. Fukami, K. Y. Camsari, H. Ohno, and S. Datta, Integer factorization using stochastic magnetic tunnel junctions, Nature **573**, 390 (2019).

[50] V. Ostwal and J. Appenzeller, Spin–orbit torque-controlled magnetic tunnel junction with low thermal stability for tunable random number generation, IEEE Magn. Lett. **10**, 4503305 (2019).

[51] P. Debashis, R. Faria, K. Y. Camsari, S. Datta, and Z. Chen, Correlated fluctuations in spin orbit torque coupled perpendicular nanomagnets, Phys. Rev. B **101**, 094405 (2020).

[52] S. Hentschke, S. Rohrer, and N. Reifschneider, in *Proceedings Ninth Annual IEEE International ASIC Conference and Exhibit* (IEEE, 1996), p. 11.

[53] D. MacNeill, G. M. Stiehl, M. H. D. Guimaraes, R. A. Buhrman, J. Park, and D. C. Ralph, Control of spin–orbit torques through crystal symmetry in WTe_2/ferromagnet bilayers, Nat. Phys. **13**, 300 (2017).

[54] D. MacNeill, G. M. Stiehl, M. H. D. Guimarães, N. D. Reynolds, R. A. Buhrman, and D. C. Ralph, Thickness dependence of spin-orbit torques generated by WTe_2, Phys. Rev. B **96**, 054450 (2017).

[55] P. Li, W. Wu, Y. Wen, C. Zhang, J. Zhang, S. Zhang, Z. Yu, S. A. Yang, A. Manchon, and X.-x. Zhang, Spin-momentum locking and spin-orbit torques in magnetic nano-heterojunctions composed of Weyl semimetal WTe_2, Nat. Commun. **9**, 3990 (2018).

[56] S. Shi, S. Liang, Z. Zhu, K. Cai, S. D. Pollard, Y. Wang, J. Wang, Q. Wang, P. He, J. Yu, G. Eda, G. Liang, and H. Yang, All-electric magnetization switching and Dzyaloshinskii–Moriya interaction in WTe_2/ferromagnet heterostructures, Nat. Nanotechnol. **14**, 945 (2019).

[57] B. Zhao, D. Khokhriakov, Y. Zhang, H. Fu, B. Karpiak, A. M. Hoque, X. Xu, Y. Jiang, B. Yan, and S. P. Dash, Observation of charge to spin conversion in Weyl semimetal WTe_2 at room temperature, Phys. Rev. Res. **2**, 013286 (2020).

[58] Y. Fan, H. Li, M. Dc, T. Peterson, J. Held, P. Sahu, J. Chen, D. Zhang, A. Mkhoyan, and J.-P. Wang, Spin pumping and large field-like torque at room temperature in sputtered amorphous WTe_{2-x} films, APL Mater. **8**, 041102 (2020).

[59] X. Li, P. Li, V. D.-H. Hou, M. DC, C.-H. Nien, F. Xue, D. Yi, C. Bi, C.-M. Lee, S.-J. Lin, W. Tsai, Y. Suzuki, and S. X. Wang, Large and Robust Charge-to-Spin Conversion in Sputtered Weyl Semimetal WTex with Structural Disorder, arXiv preprint arXiv:2001.04054 (2020).

[60] R. Shimabukuro, K. Nakamura, T. Akiyama, and T. Ito, Electric field effects on magnetocrystalline anisotropy in

ferromagnetic Fe monolayers, Physica E Low Dimens. Syst. Nanostruct. **42**, 1014 (2010).

[61] Y. Yang, H. Xie, Y. Xu, Z. Luo, and Y. Wu, Multistate Magnetization Switching Driven by Spin Current From a Ferromagnetic Layer, Phys. Rev. Appl. **13**, 034072 (2020).

[62] S.-h. C. Baek, V. P. Amin, Y.-W. Oh, G. Go, S.-J. Lee, G.-H. Lee, K.-J. Kim, M. D. Stiles, B.-G. Park, and K.-J. Lee, Spin currents and spin–orbit torques in ferromagnetic trilayers, Nat. Mater. **17**, 509 (2018).

[63] H.-Y. Lee, S. Kim, J.-Y. Park, Y.-W. Oh, S.-Y. Park, W. Ham, Y. Kotani, T. Nakamura, M. Suzuki, T. Ono, K.-J. Lee, and B.-G. Park, Enhanced spin–orbit torque via interface engineering in Pt/CoFeB/MgO heterostructures, APL Mater. **7**, 031110 (2019).

[64] K. Garello, C. O. Avci, I. M. Miron, M. Baumgartner, A. Ghosh, S. Auffret, O. Boulle, G. Gaudin, and P. Gambardella, Ultrafast magnetization switching by spin-orbit torques, Appl. Phys. Lett. **105**, 212402 (2014).

[65] Z. Luo, Y. Xu, Y. Yang, and Y. Wu, Magnetic angular position sensor enabled by spin-orbit torque, Appl. Phys. Lett. **112**, 262405 (2018).

[66] A. Grosz, V. Mor, E. Paperno, S. Amrusi, I. Faivinov, M. Schultz, and L. Klein, Planar Hall effect sensors with subnanotesla resolution, IEEE Magn. Lett. **4**, 6500104 (2013).

[67] Y. Guo, J. Wang, R. M. White, and S. X. Wang, Reduction of magnetic 1/f noise in miniature anisotropic magnetoresistive sensors, Appl. Phys. Lett. **106**, 212402 (2015).